Lithos 126 (2011) 233–247

Contents lists available at ScienceDirect

Lithos

journal homepage: www.elsevier.com/locate/lithos

Ancient sub-continental lithospheric mantle (SCLM) beneath the eastern part of the Central Asian Orogenic Belt (CAOB): Implications for crust–mantle decoupling

Yan-Long Zhang [a], Chuan-Zhou Liu [b,*], Wen-Chun Ge [a], Fu-Yuan Wu [b], Zhu-Yin Chu [b]

[a] College of Earth Sciences, Jilin university, Changchun 130026, China
[b] State Key Laboratory of Lithospheric Evolution, Institute of Geology and Geophysics, Chinese Academy of Sciences, Beijing 100029, China

ARTICLE INFO

Article history:
Received 22 December 2010
Accepted 27 July 2011
Available online xxxx

Keywords:
Crust–mantle decoupling
Mantle xenoliths
Sr–Nd–Hf–Os isotopes
Potassic basaltic rocks

ABSTRACT

Potassic basaltic lavas erupted during the Cenzoic are widespread in Wudalianchi, Erkeshan and Keluo (WEK) areas, northeast China, and contain abundant mantle xenoliths. Mantle xenoliths in this study are selected from the Keluo potassic lavas, and mainly comprise spinel lherzolites and harzburgites with minor dunites and wehrlites. Modal metasomatism is evident in some Keluo xenoliths from the presence of phlogopite and rutile. Mineral compositions indicate that the Keluo xenoliths represent mantle residues after variable degrees of melting, i.e., 1–5% for lherzolites and 3–11% for harzburgites, with subsequent refertilization. Both bulk-rock and clinopyroxene data show enrichment in light rare earth elements (LREE) and some other incompatible elements (e.g. Ba, U). Clinopyroxenes from some of the Keluo xenoliths have radiogenic Sr isotopes, but unradiogenic Nd–Hf isotopes relative to the Cenozoic mantle xenoliths from other localities of the NE China. The Keluo mantle xenoliths have variable $^{187}Os/^{188}Os$ ratios ranging from 0.11458 to 0.13194. Although most Keluo mantle xenoliths have been affected by Re addition, their Os isotope compositions have not been significantly modified. The unradiogenic $^{187}Os/^{188}Os$ ratios of the refractory harzburgites give Re depletion ages (T_{RD}) of ~1.9–2.1 Ga. This suggests that the sub-continental lithospheric mantle (SCLM) beneath the Keluo area was formed during the Paleoproterozoic, which is older than the age of the overlying crust that was mainly formed since the Neoproterozoic. Therefore, the SCLM beneath the Kelou area is temporally decoupled from the overlying crust. It is unlikely that the Cenozoic SCLM beneath the Keluo area was newly accreted from the asthenosphere, in which ancient mantle domains were preserved. We propose that the ancient mantle beneath the Keluo region is extraneous and has been emplaced from other locations.

1. Introduction

Potassic igneous rocks erupted during the Cenozoic have been well documented in the Wudalianchi, Erkeshan and Keluo (WEK) fields in the Xing'an-Mongolia Orogenic Belt (XMOB), northeast China (Liu, 1987; Zhang et al., 1995; Zou et al., 2003). They are characterized by high K_2O contents (e.g., $K_2O/Na_2O>1$) and marked enrichment in incompatible elements, especially the large ion lithophile elements (LILEs, e.g., Rb, Ba, Th, U) and light rare earth elements (LREE). These features, together with their Sr–Nd–Pb isotopes, have been explained by low degree melting of phlogopite-bearing garnet peridotites, which have been subjected to metasomatic processes as old as the Proterozoic (Zhang et al., 1998; Zou et al., 2003). This inference is also supported by the Sr–Nd isotopes of clinopyroxene from mantle xenoliths entrained in the WEK potassic rocks (Zhang et al., 2000). Therefore, both potassic rocks and mantle xenoliths indicate the existence of Proterozoic sub-continental lithospheric mantle (SCLM) beneath the WEK area during the Cenozoic. On the other hand, previous Re–Os isotope studies on mantle xenoliths from the eastern portion of NE China (e.g., Wangqing, Yitong, Shangliao and Jiaohe) have suggested that the Cenozoic SCLM is juvenile and probably represents fertile mantle accreted from the asthenosphere during the Phanerozoic (Wu et al., 2003b, 2006; Zhou et al., 2007, 2010). This implies that the SCLM beneath the WEK field is different from the neighboring areas. Furthermore, various studies on both granites and volcanic rocks have shown that the crust in the XMOB is juvenile and was mainly accreted during the Phanerozoic (Ge et al., 2007; Guo et al., 2009; Jahn et al., 2004; Sui et al., 2007; Wu et al., 2000, 2002, 2003a; Zhang et al., 2006, 2007, 2010). Therefore, it seems that the crust is decoupled from the SCLM in the WEK region, i.e., an old mantle underlies the young crust.

However, the formation age of the SCLM beneath the WEK region has been not directly constrained and so to better constrain the age of the SCLM and understand the crust–mantle decoupling, we have conducted a Re–Os isotope study on mantle xenoliths entrained in the Kelou potassic basalts. Major, trace elements and Sr–Nd–Hf isotopes of the Keluo mantle xenoliths are also presented and the history of melting and metasomatism of the SCLM in the region will be discussed.

* Corresponding author. Tel.: +86 10 82998547; fax: +86 10 62010846.
E-mail address: chzliu@mail.iggcas.ac.cn (C.-Z. Liu).

0024-4937/$ – see front matter © 2011 Elsevier B.V. All rights reserved.
doi:10.1016/j.lithos.2011.07.022

2. Geological background and sample descriptions

The Xing'an-Mongolia Orogenic Belt (XMOB) is the eastern part of Central Asian Orogenic Belt (CAOB), which is sandwiched between the Siberian and North China cratons (Jahn et al., 2000, 2004; Sengör et al., 1993). It comprises a series of micro-continents (Fig. 1a), including the Erguna Block, the Xina'an Block, the Songnen Block and the Jiamusi Massif (Ye et al., 1994). They are separated by the Tayuan-Xiguitu, Hegenshan-Nenjiang and Jiayin-Mudanjiang faults, respectively (Fig. 1a). The Erguna Massif is considered to be the eastern extension of the Central Mongolian microcontinent. Granite outcrops are common in the XMOB and have been linked to the closure of the Paleo-Asian Ocean in the Paleozoic and Paleo-Pacific during the Mesozoic. Nd isotopic data for the granitoids indicate a crustal formation age of 1680–1060 Ma (Wu et al., 2003a), which is comparable to that of the Jamusi Massif (Sui et al., 2007; Wu et al., 2000). In contrast, granites in the Xing'an and Songnen Blocks have much younger model ages, i.e., <1000 Ma (Jahn et al., 2000, 2004; Wu et al., 2000, 2002, 2003a). Similar conclusions have also been arrived using Hf isotopes from zircons in granites (Ge et al., 2007; Sui et al., 2007; Zhang et al., 2010).

Cenozoic basaltic magmatism is widely distributed in NE China (Fan and Hooper, 1989; Liu, 1992). Potassic rocks that erupted during the Late Pliocene–Pleistocene (2.3~0.13 Ma) and Quaternary (1719–1721 A.D.) are widespread in the WEK areas, i.e., Wudalianchi, Erkeshan and Keluo (Fig. 1a). The Keluo potassic rocks were erupted in the Middle Pleistocene and are composed of leucitite, olivine basalt, olivine leucitite, leucitic basanite and vitrobasalt (Liu, 1987). The olivine basalts contain abundant spinel-facies mantle xenoliths but no garnet peridotites. Samples selected in this study were collected from the Dayizishan Volcano near the Keluo town (Fig. 1b). They are mainly composed of spinel lherzolites, with minor spinel harzburgites, dunites and wehrlite (Fig. 2). Their modal contents of olivine are variable ranging from 50% to 94% (Table 1).

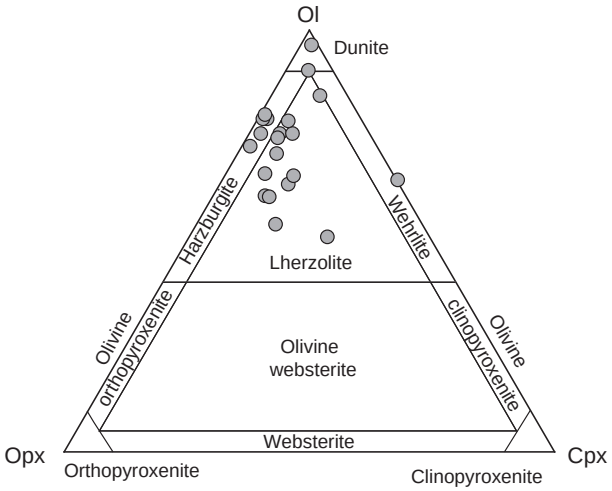

Fig. 2. Petrological classification of Keluo peridotite xenoliths.

Most Keluo mantle xenoliths are small, with a diameter of 3–8 cm (Fig. 3a). They display porphyroclastic to equigranular microstructures with little deformation (Fig. 3b–e). Triple junctions are common

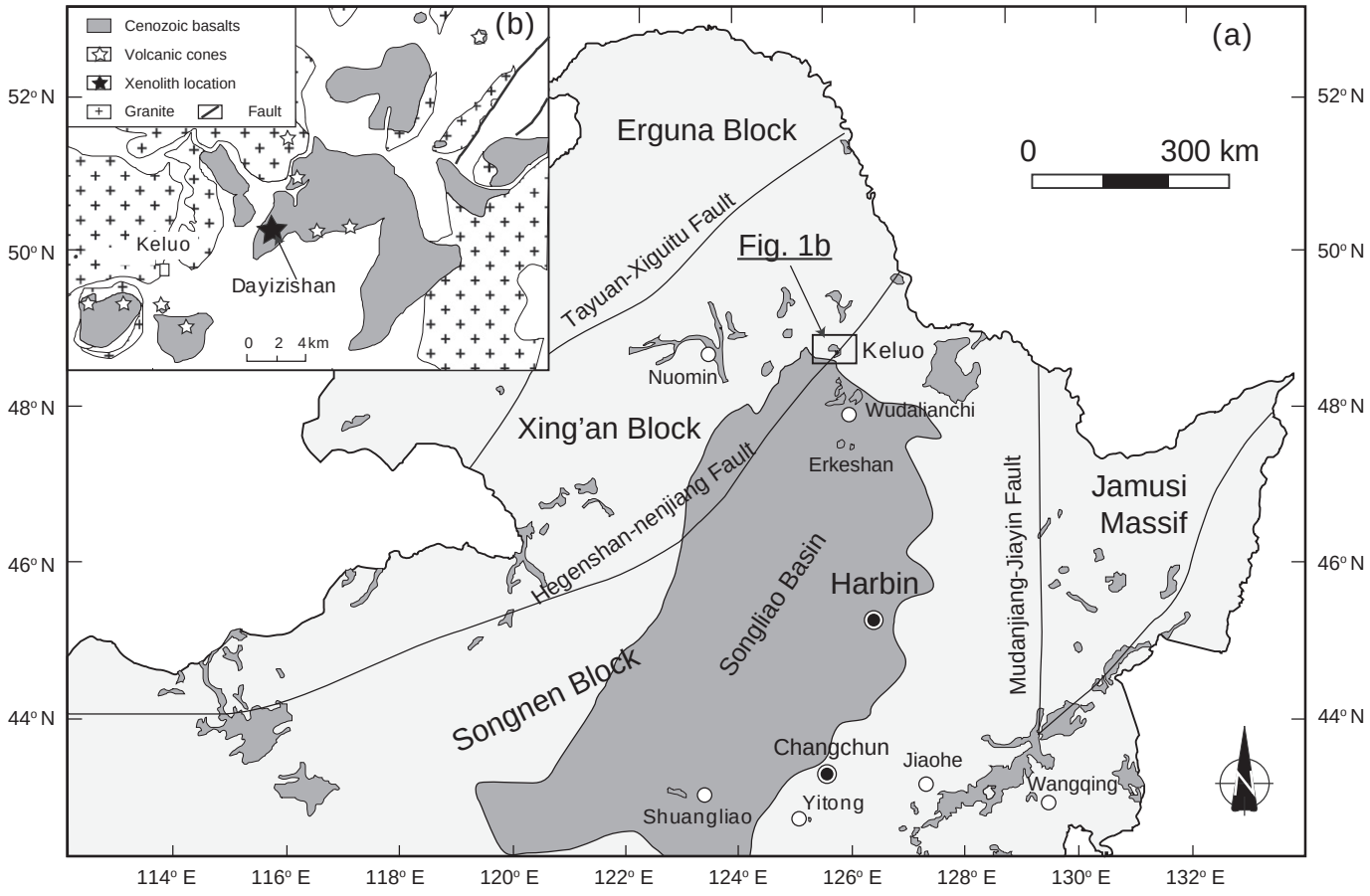

Fig. 1. Sketch map of the Northeast (NE) China, in which the distribution of the Cenozoic volcanic rocks is shown (a); the distribution of granites and volcanic rocks in the Keluo area (b).

among the neoblasts (Fig. 3b–d). Olivine porphyroclasts generally display kink-bands (Fig. 3d). The poikilitic spinel commonly shows a holly-leaf shape (Fig. 3b, c). Occasionally, round spinel is also included within olivine and orthopyroxene porphyroclasts. Round shaped olivine in the wehrlite is always surrounded by clinopyroxene (Fig. 3e). Euhedral tabular phlogopite grains have been found in two spinel peridotites (08KL-01 and 08KL-11). Phlogopite veins occur in sample 08KL-11 (Fig. 3f), in which rutile has also been observed but with a modal content less than 0.1%.

3. Analytical methods

Whole rock major and trace elements were measured at the Guangzhou Institute of Geochemistry, Chinese Academy of Sciences (GIGCAS). Mineral compositions, clinopyroxene Sr–Nd–Hf isotopes, highly siderophile elements (HSE) and Re–Os isotopes were finished at the Institute of Geology and Geophysics, Chinese Academy of Sciences (IGGCAS).

3.1. Whole rock major and trace elements

Whole rock major elements were determined by X-Ray fluorescence (XRF) method, as described in Li et al. (2006). Samples were prepared as glass disks using Rigaku desktop fusion machine, produced by mixing 0.5 g of rock powder (dried at 110 °C) with 4.0 g of lithium tetraborate for 15 min at 1100 °C in Pt–Au crucibles. Major elements were determined on a Rigaku ZSX100e instrument with an analytical uncertainty of 1%–5%.

Whole rock trace elements were measured by inductively coupled plasma mass spectrometry (ICP-MS), using a Perkin-Elmer Sciex Elan 6000 instrument. The detailed procedure has been given in Li et al. (2006). The precision for minor and trace elements is better than 5%.

3.2. Mineral major and trace elements

Mineral major elements were measured using a JEOL-JXA8100 electron microprobe with an accelerating voltage of 15 kV and current of 12 nA in a wavelength-dispersive (WDS) mode. Trace elements of clinopyroxene were analyzed using a laser ablation inductively-coupled mass spectrometer (LA-ICP-MS). The detailed description of the method has been given in Liu et al. (2010a). The laser ablation ICP-MS system consists of a Lambda Physik LPX 120I pulsed ArF excimer laser coupled to an Agilent 7500 ICP-MS. A glass standard, NIST 610, was used as an external calibration standard. Calcium (^{43}Ca) was selected as an internal standard. The CaO contents of NIST 610 used in calculation is 11.45%, and the reference data is from Pearce et al. (1997). The data were reduced using the GLITTER 4.0 developed by GEMOC, Macquarie University (Griffin et al., 2008).

3.3. Clinopyroxene Sr–Nd–Hf isotopes

The separated clinopyroxene was ground to 200–400 meshes using an agate mortar after being washed in ultra-pure (milli-Q) water. About 150 mg of clinopyroxene powder and mixed isotopic tracers (i.e., ^{87}Rb-^{84}Sr, ^{149}Sm-^{150}Nd and ^{176}Lu-^{180}Hf) were added into a 7 ml round-bottom Savillex™ Teflon crew-top capsule. The samples were dissolved using a mixed acid of 2 ml HF and 0.2 ml $HClO_4$ on a hotplate at 120 °C for about 1 week. After the samples were completely dissolved, the solutions were dried on hotplate at 150 °C to remove the HF and $HClO_4$. 3 ml HCl was added to the residue, and then dried. Finally, the residue was dissolved in 5 ml of 3 M HCl, and placed on a hotplate at ~100 °C overnight prior to column separation. The sample solution was centrifuged and then sequentially loaded onto pre-conditioned LN (LN-C-50A, 2 ml) chromatographic columns, AG50W-X12 (2 ml) cation exchange columns and another commercial LN (LN-C-50B, 2 ml) Spec resin column for separating the Lu, Hf, Rb, Sr, Nd and Sm. A combined procedure for separating Lu, Hf, Rb, Sr, Sm and Nd from a single sample digestion was used (Chu et al., 2009; Yang et al., 2010).

Both Rb–Sr and Sm–Nd isotopes were determined using an Isoprobe-T thermal ionization mass spectrometer (TIMS). Measured $^{87}Sr/^{86}Sr$ and $^{143}Nd/^{144}Nd$ ratios were mass fractionation corrected using $^{86}Sr/^{88}Sr = 0.1194$ and $^{146}Nd/^{144}Nd = 0.7219$, respectively. During the period of data collection, the measured values for the NBS-987 Sr standard and the JNdi-Nd standard are $^{87}Sr/^{86}Sr = 0.710250 \pm 11$ ($n = 18$) and $^{143}Nd/^{144}Nd = 0.512120 \pm 12$ ($n = 12$), respectively. Both Lu and Hf isotopes were measured using a Thermo-Electron Neptune multi-collector ICP-MS (MC-ICPMS). Hafnium isotopic ratios were normalized to $^{179}Hf/^{177}Hf = 0.7325$ and $^{176}Lu/^{175}Lu$ isotopic ratios were normalized using the Yb isotopic ratios. The measured $^{176}Hf/^{177}Hf$ ratios of the JMC475 are 0.282165 ± 10 ($n = 10$). In addition, the USGS reference materials BCR-1 and BHVO-2 were also analyzed for Sr–Nd–Hf isotopes. The obtained $^{87}Sr/^{86}Sr$, $^{143}Nd/^{144}Nd$ and $^{176}Hf/^{177}Hf$ ratios for BCR-1 are 0.704977 ± 12, 0.512655 ± 5 and 0.282866 ± 6, respectively, whereas those of BHVO-2 are 0.703474 ± 11, 0.513000 ± 15 and 0.283109 ± 5, respectively.

3.4. Highly siderophile elements and Re–Os isotopes

Highly siderophile elements (HSE) and Re–Os isotopes were measured by isotope dilution methods following the procedure described by Chu et al. (2009). The KL-series samples have only measured the Re–Os isotopes. About 2 g powder together with Re–Os (^{187}Re and ^{190}Os) and reverse aqua regia (3 ml 12 N HCl and 6 ml 15 N HNO_3) were digested in a Carius Tube at 240 °C for 48–72 h. Both HSE and Re–Os isotopes were determined for 08KL-series samples, for which HSE (^{99}Ru, ^{105}Pd, ^{191}Ir and ^{194}Pt) isotope tracers were also added together with Re–Os isotope tracers. Osmium was extracted from the aqua regia solution by CCl_4 and further purified by micro-distillation using the method described by Birck et al. (1997). For KL-series samples, Re was extracted from the solution by anion exchange chromatography using 2 ml resin (AG-1×8, 100–200 meshes). For 08KL-series samples, Ru, Pd, Re, Ir and Pt were sequentially separated from the solution by anion exchange method.

Osmium concentrations and isotopic ratios were measured by N-TIMS on a GV Isoprobe-T instrument in a static mode using the Faraday cups. The $Ba(OH)_2$ solution was used as ion emitter. The measured Os isotopic ratios were corrected for mass fractionation using $^{192}Os/^{188}Os = 3.0827$. The in-run precisions for Os isotopic measurements were better than 0.2% (2δ; δ = relative standard deviation) for all the samples. The Jahnson–Matthey standard of UMD was used as an external standard and its ratio is 0.11378 ± 2 during the experiments in this study. The concentrations of Ir, Ru, Pt, Pd and Re were measured on a Thermal-Electron Neptune MC-ICPMS in a peak-jumping or static mode, according to their measured signal intensity. In-run precisions for $^{185}Re/^{187}Re$, $^{191}Ir/^{193}Ir$, $^{99}Ru/^{101}Ru$, $^{194}Pt/^{196}Pt$ and $^{105}Pd/^{106}Pd$ were typically 0.1–0.3% (2δ). The total procedural Os blank was 3–5 pg with $^{187}Os/^{188}Os$ of about 0.15, which was negligible for all samples in this study. Total procedural blanks were about 3 pg for Re, 7 pg for Ir, 7 pg for Ru, 4 pg for Pt and 4 pg for Pd. The blank corrections were negligible (<1%) for Ir, Ru, Pt and Pd, but as great as 10–30% for Re for the low-Re samples. The standard WPR-1 was analyzed to monitor the reliability of the method, and the obtained results agree within analytical errors with the reference values (GEOREM: http://georem.mpch-mainz.gwdg.de).

4. Results

4.1. Whole-rock compositions

Bulk-rock major and trace element compositions are listed in Table 1. Most samples are fresh and have low loss on ignition (LOI) values, which is consistent with petrographic observations. The

Table 1
Whole rock major and trace element compositions of the Keluo mantle xenoliths. Lz: lherzolite; Hz: harzburgite; D: dunite; W: wehrlite. Mineral modal contents were estimated by method described in Herrmann and Berry (2002).

Sample	BHVO-1	AGV-2	KL3-24	KL3-26	KL3-27-1	KL3-27-2	KL3-28	KL3-30	KL3-31	KL3-38	KL3-40	KL3-41
Lithology	standard		Hz	Lz	Lz	D	Lz	Hz	Lz	Lz	Hz	Hz
Modal contents (vol.%)												
Ol			74.1	63.4	50.3	93.6	60.3	77.9	64.7	74.3	78.6	71.2
Cpx			2.3	14.0	27.8	2.3	10.7	1.7	7.8	6.2	0.8	1.8
Opx			22.1	20.1	21.1	1.5	28.9	19.5	26.2	18.3	18.9	25.6
Sp			1.3	2.3	1.0	1.3	0.0	0.3	2.0	1.7	1.5	0.6
Phl			0	0	0	0	0	0	0	0	0	0
Rt			0	0	0	0	0	0	0	0	0	0
Major elements (wt.%)												
SiO2	49.79	59.57	43.82	44.45	46.16	39.52	43.92	43.80	44.41	43.43	43.71	44.32
MgO	7.17	1.76	45.34	40.59	36.21	46.06	40.13	45.61	41.97	43.81	46.18	44.27
Al2O3	13.69	16.62	1.28	2.66	2.69	0.73	3.31	0.74	2.70	1.74	0.77	1.35
Fe2O3	12.37	6.92	8.14	8.46	7.48	12.89	8.91	9.07	8.48	9.12	8.20	8.78
TiO2	2.73	1.06	0.06	0.07	0.33	0.08	0.10	0.02	0.07	0.04	0.04	0.07
CaO	11.32	5.13	0.55	3.17	6.24	0.37	3.05	0.44	1.83	1.40	0.43	0.47
MnO	0.16	0.10	0.11	0.11	0.11	0.14	0.12	0.11	0.11	0.11	0.10	0.10
K2O	0.51	2.89	0.09	0.03	0.03	0.04	0.01	0.02	0.04	0.02	0.13	0.03
Na2O	2.14	4.14	0.10	0.17	0.28	0.03	0.16	0.03	0.12	0.07	0.10	0.07
P2O5	0.26	0.47	0.03	0.01	0.01	0.02	0.01	0.01	0.02	0.01	0.02	0.01
LOI	0.16	1.18	−0.15	−0.32	−0.08	−0.69	−0.34	−0.52	−0.36	−0.39	−0.28	−0.11
Total	100.31	99.84	99.38	99.40	99.46	99.19	99.38	99.34	99.39	99.35	99.38	99.36
Trace elements (ppm)												
Sc	32	12	7	16	23	5	15	6	12	9	7	36
Ti	16,932	6556	336	354	1556	359	485	108	343	216	209	796
V	319	119	35	63	130	36	76	23	73	39	35	165
Cr	290	21	3330	4034	3869	10,566	3962	3429	4461	3672	4312	4660
Co	45	16	100	98	85	144	103	104	98	112	108	76
Ni	121	20	2317	2060	1731	2438	2105	2358	2181	2353	2560	1737
Cu	139.02	57.90	2.39	11.93	27.32	5.44	6.01	1.63	8.12	3.31	2.10	29.84
Rb	10.48	67.42	1.74	0.41	0.53	0.62	0.15	0.41	0.48	0.31	1.89	0.17
Sr	409.1	640.3	21.7	18.3	22.2	14.9	13.9	7.2	18.2	9.7	13.2	31.4
Y	26.6	19.3	0.8	2.2	3.8	0.3	2.8	0.3	1.4	0.8	0.4	5.8
Zr	185.8	218.2	8.0	4.9	11.5	4.1	4.5	2.8	3.8	2.9	4.3	7.8
Nb	18.64	14.02	1.12	0.32	0.59	0.67	0.12	0.33	0.33	0.17	0.88	0.17
Ba	138.0	1122.7	25.0	11.7	9.0	13.3	8.7	7.9	21.3	7.3	17.9	13.9
La	14.2	39.1	1.7	1.4	1.2	1.8	0.6	0.5	1.5	0.6	1.0	1.6
Ce	39.12	69.46	3.70	2.57	3.47	3.11	1.47	1.02	2.31	1.18	2.07	4.25
Pr	5.41	8.08	0.40	0.32	0.59	0.29	0.24	0.13	0.25	0.16	0.25	0.70
Nd	27.06	33.87	1.55	1.36	3.05	0.89	1.16	0.51	0.94	0.69	0.90	3.44
Sm	6.29	5.88	0.27	0.35	0.86	0.12	0.35	0.10	0.20	0.16	0.17	0.97
Eu	2.09	1.45	0.08	0.12	0.28	0.04	0.12	0.03	0.07	0.05	0.05	0.31
Gd	6.15	4.84	0.25	0.39	0.90	0.12	0.41	0.09	0.23	0.16	0.15	1.11
Tb	1.01	0.69	0.03	0.06	0.14	0.01	0.08	0.01	0.04	0.02	0.02	0.18
Dy	5.45	3.71	0.14	0.41	0.79	0.06	0.48	0.07	0.25	0.15	0.10	1.09
Ho	0.97	0.69	0.03	0.08	0.15	0.01	0.11	0.01	0.06	0.03	0.02	0.23
Er	2.61	1.88	0.07	0.22	0.36	0.03	0.30	0.03	0.16	0.09	0.04	0.61
Tm	0.35	0.26	0.01	0.03	0.05	0.00	0.05	0.01	0.03	0.01	0.01	0.09
Yb	2.13	1.76	0.08	0.23	0.30	0.03	0.31	0.03	0.18	0.11	0.04	0.57
Lu	0.31	0.27	0.01	0.04	0.05	0.01	0.05	0.01	0.03	0.02	0.01	0.09
Hf	4.48	5.16	0.18	0.13	0.45	0.09	0.14	0.05	0.10	0.06	0.10	0.33
Ta	1.23	0.95	0.06	0.02	0.04	0.03	0.01	0.02	0.02	0.01	0.04	0.01
Pb	2.46	35.00	0.54	1.42	0.27	0.31	0.36	0.84	0.62	0.09	0.63	0.55
Th	1.47	6.78	0.15	0.14	0.09	0.11	0.04	0.04	0.10	0.03	0.12	0.09
U	0.42	1.82	0.03	0.06	0.03	0.03	0.03	0.02	0.07	0.02	0.03	0.05

lherzolites contain 1.57–3.99 wt.% Al_2O_3 and 1.29–6.24 wt.% CaO, whereas the harzburgites and dunites have lower contents of both Al_2O_3 and CaO, i.e., ~0.65–1.35 wt.% vs. ~0.37–0.95 wt.%, respectively. The wehrlite (08KL-07) contains the lowest MgO (37.63 wt.%) and highest CaO (6.97 wt.%). The bulk TiO_2 contents are 0.05–0.41 wt.% in lherzolites, 0.02–0.07 wt.% in harzburgites, 0.03–0.08 wt.% in dunites and 0.16 wt.% in the wehrlite. For most xenoliths, the MgO contents show negative correlation with both Al_2O_3 and CaO contents (Fig. 4a, b). Due to their high modal contents of clinopyroxene (28 vol.% vs. 35 vol.%, respectively), both lherzolite KL3-27-1 and wehrlite 08KL-07 deviate from the correlations to higher CaO and MgO contents. Four clinopyroxene-poor lherzolites, harzburgites and dunites plot in the field of the depleted cratonic mantle, whereas other lherzolites are plotted along the oceanic trend (Fig. 4c).

The Keluo mantle xenoliths display three different bulk-rock rare earth element (REE) patterns. The fertile lherzolites show flat REE patterns with a slight enrichment in light rare earth elements (LREE; Fig. 5a). Two phlogopite-bearing lherzolites (08KL-01 and 08KL-11) display different REE patterns: sample 08KL-01 has a REE pattern similar to those of the phlogopite-free lherzolites, whereas sample 08KL-11 displays fractionated REE pattern with a $(La/Yb)_n$ (n: chondrite normalized) of 10.6. Both harzburgites and dunites are enriched in LREE but display flat patterns in heavy rare earth element (HREE; Fig. 5b). The harzburgite KL3-41 is distinguished from other

08KL-01	08KL-02	08KL-03	08KL-04	08KL-05	08KL-07	08KL-09	08KL-10	08KL-11	08KL-12	08KL-13
Lz	Hz	Lz	Lz	Lz	W	Lz	Lz	Lz	Lz	D
73.1	78.1	58.2	68.5	74.0	64.0	52.7	61.6	77.5	76.4	90.8
6.4	1.2	11.3	8.0	8.8	35.0	16.0	13.8	8.7	6.4	4.1
19.3	20.0	27.5	21.0	15.9	0.0	29.7	22.1	5.1	15.1	4.7
1.7	0.0	3.0	3.0	1.9	1.1	3.0	3.0	0.0	1.9	0.4
<0.1	0	0	0	0	0	0	0	8.9	0	0
0	0	0	0	0	0	0	0	<0.1	0	0
44.10	43.88	44.54	43.32	43.31	45.66	44.88	43.76	43.64	42.75	42.08
43.27	45.54	39.44	42.19	43.08	37.63	37.80	39.84	43.69	44.05	46.96
1.93	0.94	3.48	2.95	1.95	1.82	3.99	3.50	1.57	1.83	0.65
8.43	7.94	8.78	8.94	9.21	6.86	9.21	8.90	7.70	9.20	8.80
0.06	0.04	0.14	0.08	0.05	0.16	0.15	0.12	0.41	0.06	0.03
1.29	0.63	2.85	1.77	1.83	6.97	3.30	3.01	1.70	1.29	0.95
0.12	0.11	0.12	0.12	0.11	0.09	0.12	0.11	0.10	0.11	0.10
0.02	0.18	0.03	0.03	0.02	0.03	0.05	0.02	0.36	0.07	0.03
0.08	0.13	0.19	0.09	0.11	0.23	0.20	0.18	0.15	0.10	0.05
0.01	0.01	0.01	0.01	0.01	0.01	0.01	0.01	0.02	0.02	0.01
0.10	−0.02	−0.19	−0.13	−0.32	0.03	−0.31	−0.09	0.06	−0.13	−0.31
99.39	99.39	99.39	99.36	99.38	99.49	99.39	99.38	99.40	99.35	99.34
11	8	15	13	13	26	17	15	12	11	7
259	208	695	373	294	877	745	611	1999	324	172
52	38	93	63	58	91	89	75	64	47	30
4043	4176	4120	3346	5032	6259	3942	4480	3894	4677	4557
103	108	106	109	117	94	104	108	112	122	128
2178	2503	2188	2260	2596	2146	1972	2212	2736	2574	2833
2.73	2.87	7.32	5.31	7.00	23.65	6.29	13.72	18.22	7.94	5.41
0.37	2.49	0.54	0.44	0.40	0.35	0.84	0.33	4.95	1.31	0.49
7.4	9.1	12.2	8.3	11.8	35.1	19.6	12.1	50.6	27	13.4
0.9	0.5	2.8	1.4	1.5	3.8	3.0	2.9	1.9	1.0	0.7
3.1	3.8	6.6	3.9	4.2	18.9	7.8	5.0	18.9	5.8	4.8
0.32	1.83	0.46	0.37	0.37	0.17	0.52	0.29	3.26	0.71	0.31
7.7	19.7	10.1	6.0	8.8	10.0	21.1	5.8	106	44.2	9.6
0.4	0.9	0.6	0.5	0.7	1.7	1.2	0.4	1.8	2.5	1.0
1.01	2.03	1.50	1.10	1.37	5.16	2.39	1.06	5.50	3.69	1.64
0.14	0.25	0.24	0.16	0.18	1.02	0.33	0.18	0.95	0.39	0.18
0.62	0.87	1.35	0.73	0.73	5.46	1.55	0.89	4.62	1.43	0.66
0.16	0.15	0.41	0.20	0.18	1.35	0.41	0.28	0.99	0.29	0.16
0.05	0.05	0.13	0.07	0.06	0.40	0.14	0.11	0.30	0.09	0.05
0.16	0.15	0.47	0.23	0.21	1.17	0.49	0.40	0.85	0.28	0.17
0.03	0.02	0.08	0.04	0.04	0.17	0.09	0.08	0.11	0.04	0.03
0.16	0.09	0.51	0.25	0.27	0.85	0.57	0.55	0.49	0.21	0.15
0.04	0.02	0.11	0.06	0.06	0.15	0.13	0.12	0.08	0.04	0.03
0.10	0.04	0.31	0.16	0.17	0.37	0.36	0.32	0.17	0.10	0.07
0.02	0.01	0.05	0.03	0.03	0.05	0.05	0.05	0.02	0.02	0.01
0.11	0.04	0.33	0.18	0.18	0.31	0.36	0.34	0.12	0.12	0.07
0.02	0.01	0.05	0.03	0.03	0.05	0.06	0.06	0.02	0.02	0.01
0.08	0.10	0.22	0.12	0.11	0.46	0.24	0.16	0.58	0.15	0.14
0.02	0.07	0.03	0.02	0.02	0.02	0.03	0.02	0.22	0.04	0.02
0.35	0.66	0.40	0.15	0.15	0.86	0.42	0.19	2.46	2.20	10.52
0.04	0.13	0.06	0.05	0.04	0.10	0.07	0.03	0.09	0.16	0.09
0.01	0.02	0.01	0.01	0.01	0.07	0.05	0.01	0.02	0.11	0.02

harzburgites by its flat REE pattern; its HREE contents are distinctly higher than other harzburgites. The wehrlite 08KL-07 shows an inverse spoon-shaped REE pattern and has higher HREE contents than most harzburgites and dunites (Fig. 5b).

All the Keluo mantle xenoliths show variable enrichment in large ion lithophile elements (LILEs; e.g., Rb, Ba, U). The lherzolites commonly show significant negative Nb, Ta and Ti anomalies (Fig. 5c). In contrast, the phlogopite-bearing lherzolite 08KL-11 shows positive Nb and Ta anomalies (Fig. 5c). The harzburgites, dunites and wehrlite show a clear negative Ti anomaly, (Fig. 5d). Both dunites and wehrlite have negative Nb and Ta anomalies, whereas the harzburgites display either positive or negative Nb and Ta anomalies (Fig. 5d).

4.2. Mineral compositions and equilibrium temperatures

Mineral major and trace element compositions of Keluo mantle xenoliths are given in Appendix Table S1 and Table S2, respectively.

4.2.1. Olivine

Olivine in the Keluo xenoliths has a forsterite content [Fo; $=100\times$ Mg/(Mg + Fe)] of 88.2–91.8. The lherzolites have lower olivine Fo than the harzburgites, i.e., ~88.1–90.8 and. 90.8–91.8, respectively. Both dunites, KL3-27-2 and 08KL-13, have different Fo contents, i.e., 88.5 and 90.3, respectively. Olivine in the wehrlite has a Fo of 90.7. In the olivine Fo vs. modal content diagram (Fig. 4d), no Keluo mantle

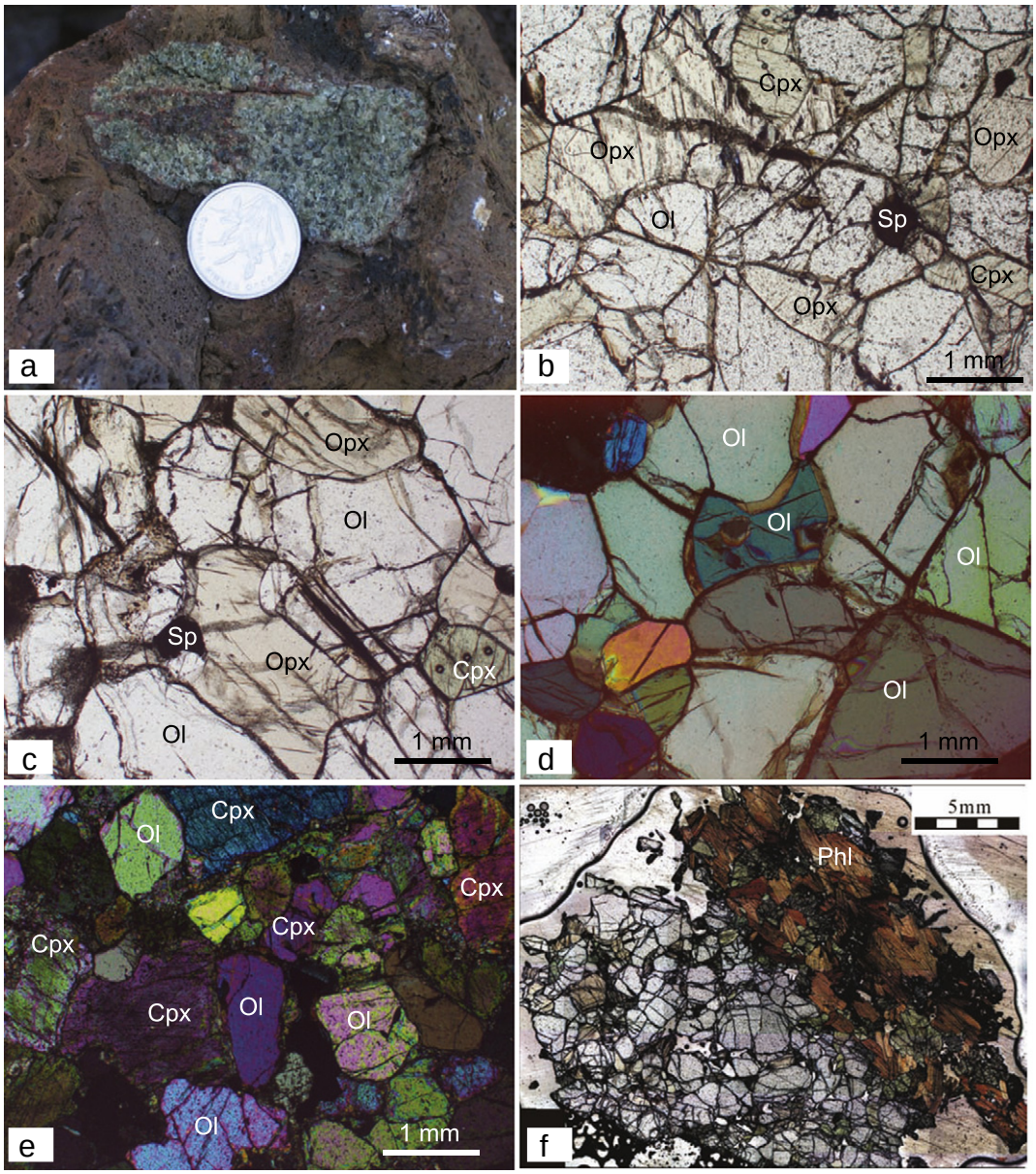

Fig. 3. Microtextures of the Keluo mantle xenoliths. (a) a hand specimen photo in the field. (b) porphyroclastic texture shown in the lherzolites (08KL-04), in which olivine is commonly anhedral and surrounded by orthopyroxene porphyclasts. (c) porphyroclastic texture shown in the harzburgites (KL3-24), in which olivine is commonly euhedaral and clinopyroxene displays poikilitic texture. (d) porphyroclastic texture shown in the dunites (KL3-27-2), in which olivine shows weak kink-band. (e) equigranular texture shown by the wehrlite (08KL-07), in which the round olivine is surrounded by clinopyroxene. (f) phlogopite veinlets in the lherzolite 08KL-11. Ol: olivine; Opx: orthopyroxene; Cpx: clinopyroxene; Sp: spinel; Phl: phlogopite.

xenoliths fall within the Archean field. Two harzburgites and three lherzolites plot within the Proterozoic field, but most lherzolites plot outside the Phanerozoic field. Two dunites clearly deviate from the oceanic trend to low olivine Fo but high modal olivine contents. Olivine from the lherzolites and harzburgites has NiO contents of 0.32–0.41 wt.% and 0.36–0.41 wt.%, respectively. The NiO contents of two dunites, KL3-27-2 and 08KL-13, are 0.35 wt.% and 0.4 wt.%, respectively. Olivine in the wehrlite contains 0.39 wt.% NiO.

4.2.2. Orthopyroxene

Orthopyroxene from the Keluo mantle xenoliths has Mg# [=Mg/(Mg+Fe)] varying from 0.89 to 0.93. The ratios of the olivine/orthopyroxene Mg# in all samples are close to unity, suggesting equilibrium in all xenoliths. Orthopyroxene of the lherzolites contains 2.27–4.40 wt.% Al_2O_3 and 0.25–1.06 wt.% CaO, whereas those of the harzburgites have 1.88–3.73 wt.% Al_2O_3 and 0.41–0.86 wt.% CaO. Orthopyroxene of both dunites contains 1.01–2.11 wt.% Al_2O_3 and 0.14–0.39 wt.% CaO.

4.2.3. Clinopyroxene

Clinopyroxene from the lherzolites has lower Mg# than those of the harzburgites, i.e., 0.89–0.92 and 0.92–0.94, respectively. Clinopyroxene from both dunites has Mg# of 0.87 and 0.93, whereas that of the wehrlite has Mg# of 0.93. Clinopyroxene from the lherzolites contains 3.89–6.34 wt.% Al_2O_3, 0.32–0.9 TiO_2 and 0.93–1.4 wt.% Na_2O, whereas those of the harzburgites are 0.76–4.93 wt.%, 0.11–0.51 wt.% and 0.53–1.17 wt.%, respectively. Clinopyroxene of dunites contains 3.15–6.47 wt.% Al_2O_3, 0.31–0.82 TiO_2 and 1.02–1.49 wt.% Na_2O, whereas clinopyroxene of the wehrlite has Al_2O_3, TiO_2 and Na_2O contents of 3.24 wt.%, 0.45 wt.% and 0.66 wt.%, respectively.

Clinopyroxene from the phlogopite-free lherzolites display consistent and flat REE patterns (Fig. 6a) and show negative anomalies of Ba,

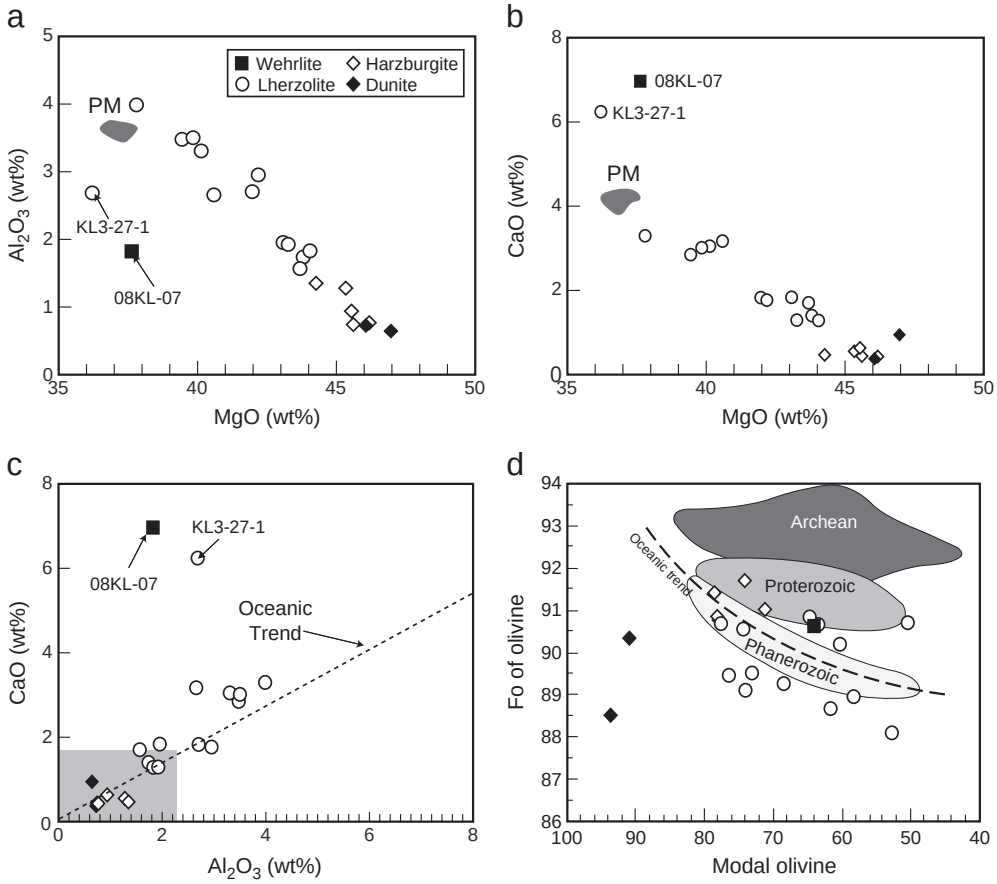

Fig. 4. Whole rock major element compositions of the Keluo mantle xenoliths. (a) MgO vs. Al_2O_3; (b) MgO vs. CaO; (c) Al_2O_3 vs. CaO, in which the depleted area is shown for comparison (Boyd, 1989; Griffin et al., 1998); (d) olivine modal content vs. Fo, in which the Arhcean, Proterozoic and Phanerozoic shown for comparison are from (Boyd, 1989; Griffin et al., 1998). PM: primitive mantle.

Nb, Ta, Zr, Hf and Ti (Fig. 6b). However, the contents of both LREE and MREE (middle rare earth elements) are distinctly higher in the phlogopite-bearing lherzolite (08KL-11) than other lherzolites (Fig. 6a). Clinopyroxene in both harzburgites and wehrlite show enrichment in LREE (Fig. 6c), and display negative Nb, Ta, Zr, Hf and Ti anomalies (Fig. 6d). Clinopyroxene in both dunites displays different REE pattern. Clinopyroxene in sample 08KL-13 shows a LREE-enriched pattern that is similar to those of the harzburgites, whereas clinopyroxene from sample KL3-27-2 has LREE and MREE contents distinctly lower than those of the harzburgites (Fig. 6c).

4.2.4. Spinel

Spinel from the Keluo mantle xenoliths has variable compositions, with Cr#[=Cr/(Cr+Al)] values of 0.08–0.54 for the lherzolites, 0.14–0.75 for the harzburgites, 0.48–0.61 for the dunites and 0.42 for the wehrlite. Spinel from the lherzolites contains 0.01–1.60 wt.% TiO_2, whereas in the harzburgites it contains 0.03–0.74 wt.% TiO_2. Spinel in dunite KL3-27-2 has the highest TiO_2 content (1.64 wt.%) among the Keluo mantle xenoliths, whereas the other dunite (08KL-13) contains 0.29 wt.% TiO_2. Spinel in the wehrlite has a TiO_2 content of 0.46 wt.%.

4.2.5. Phlogopite and rutile

Phlogopite from the Keluo mantle xenoliths has Mg# of 0.92 within the range of mantle phlogopite. It also contains 2.58–3.71 wt.% TiO_2 and 9.41–9.55 wt.% K_2O, supporting its metasomatic origin. Rutile only occurs in sample 08KL-11, and contains 86.38 wt.% TiO_2, 6.34 wt.% FeO and 6.13 wt.% MgO. Trace elements have been measured for phlogopite, which shows fractionated REE patterns and clear positive anomalies in Rb, Ba, Sr and Ti (Fig. 7a, b).

4.3. Clinopyroxene Sr–Nd–Hf isotopes

The Rb–Sr, Sm–Nd and Lu–Hf isotopic compositions of the clinopyroxene are listed in Table 2. Clinopyroxene in most samples has $^{87}Rb/^{86}Sr$ ratios less than 0.02 and $^{87}Sr/^{86}Sr$ ratios varying between 0.703635 and 0.706267. Although it has the highest $^{87}Rb/^{86}Sr$ ratio (0.118), clinopyroxene of sample 08KL-09 does not have the highest $^{87}Sr/^{86}Sr$ ratio (0.704416). $^{143}Nd/^{144}Nd$ ratios range from 0.51264 to 0.51303, giving ε_{Nd} values between −0.1 and +7.6. The Nd isotopes of most xenoliths give Proterozoic model ages (0.57–2.31 Ga), whereas two samples give model ages close to, or even greater than, the age of the Earth. Clinopyroxene of the Keluo xenoliths shows no correlation between $^{87}Sr/^{86}Sr$ and ε_{Nd} (Fig. 8a). Clinopyroxene of all but sample 08KL-13 has $^{176}Hf/^{177}Hf$ ratios that vary from 0.282839 to 0.283884 (Fig. 8b), giving a ε_{Hf} range of +2.4~+39.3. Clinopyroxene from sample 08KL-13 has the lowest $^{176}Hf/^{177}Hf$ ratio of 0.282548 among the Keluo xenoliths, giving a ε_{Hf} of −7.9. Both Nd and Hf isotopes of clinopyroxene in 08KL-13 give similar model ages of 1.28 Ga.

4.4. Highly siderophile elements (HSEs) and Re–Os isotopes

The HSE and Re–Os isotopic data of the Keluo xenoliths are given in Table 3. The Keluo mantle xenoliths contain 0.28–3.79 ppb Os, 0.83–1.81 ppb Ir, 1.57–4.21 ppb Ru, 1.81–9.35 ppb Pt, 0.23–6.84 ppb Pd and 0.002–1.731 ppb Re. Most Keluo xenoliths have sub-chondritic Os/Ir ratios, with $(Os/Ir)_n$ (n: chondrite-normalized; (McDonough and Sun, 1995)) ratios of 0.87–1.03. Both 08KL-05 and 08KL-07 have suprachondritic Os/Ir ratios, with $(Os/Ir)_n$ ratios of 1.65 and 1.67, respectively. The Ru/Ir ratios of almost all Keluo mantle xenoliths are

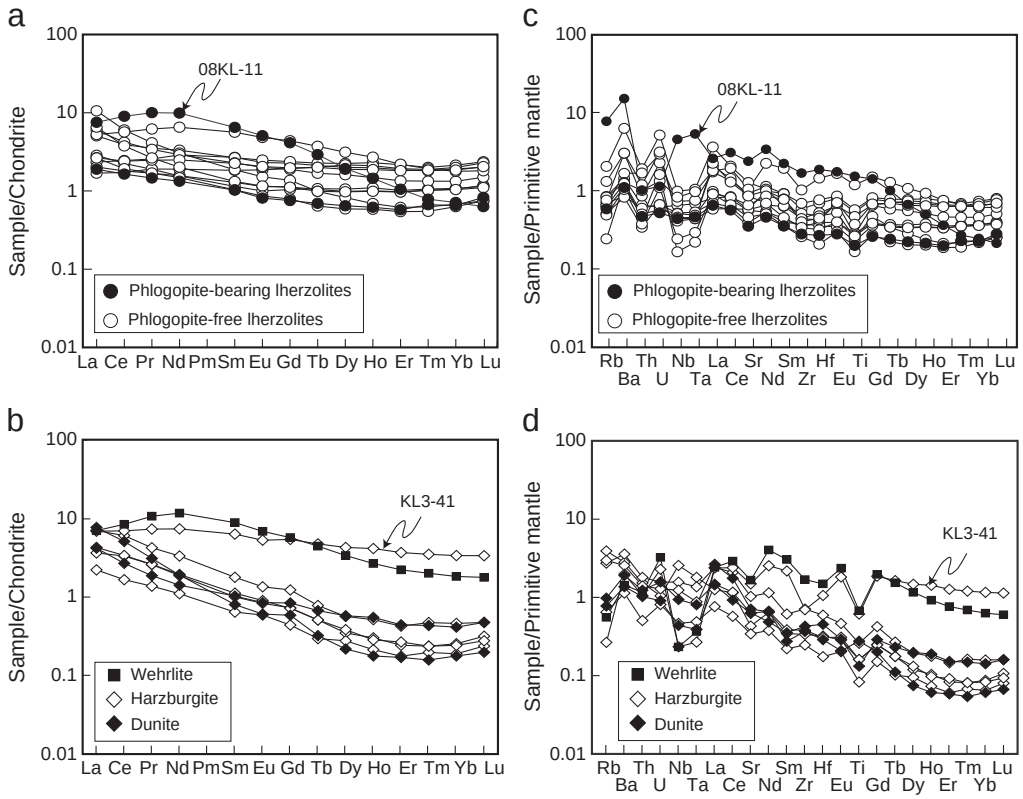

Fig. 5. Whole rock chondrite-normalized REE patterns (a, b) and primitive mantle-normalized element patterns (c, d) of the Keluo mantle xenoliths. The normalization values of both chondrite and primitive mantle are from Sun and McDonough (1989).

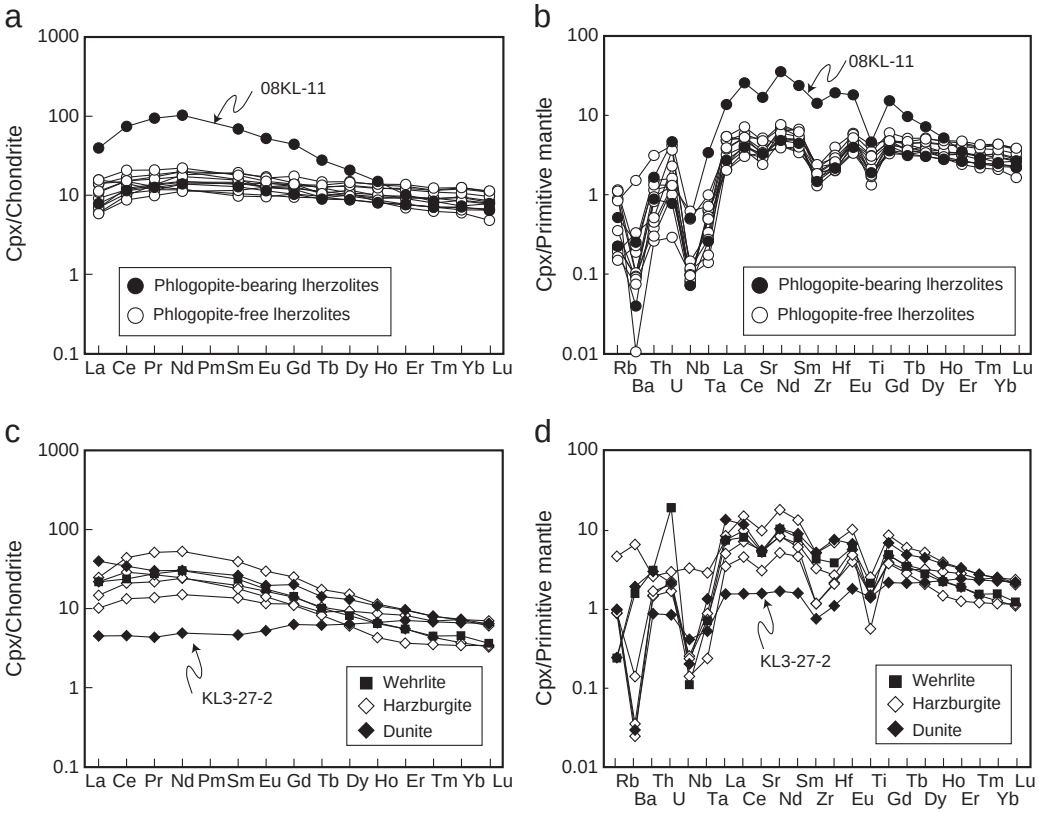

Fig. 6. Chondrite-normalized rare earth element patterns (a, b) and primitive mantle-normalized element patterns (c, d) for clinopyroxenes from Keluo mantle xenoliths.

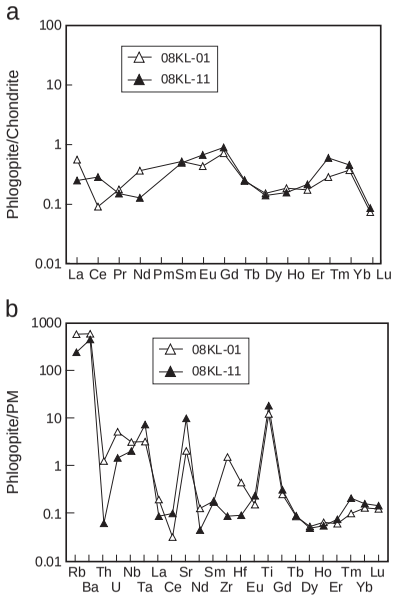

Fig. 7. Chondrite-normalized REE patterns (a) and primitive mantle-normalized element patterns (b) for phlogopite of Keluo mantle xenoliths.

suprachondritic, which has been suggested to be a feature of the upper mantle (Becker et al., 2006; Liu et al., 2009). The lherzolites have relatively flat patterns from Os to Pd, but display a big variation in Re (Fig. 9a). Three lherzolites (08KL-04, 08KL-05 and 08KL-12) show depletion in Re relative to Pd, whereas other lherzolites show variable enrichment of Re over Pd. The phlogopite-bearing lherzolite (08KL-11) has the highest Re content up to 1.731 ppb. The harzburgite (08KL-02) and dunite (08KL-13) show depletion of both Pt and Pd relative to Os, Ir and Ru, whereas the wehrlite (08KL-02) displays a flat pattern from Os to Pd (Fig. 9b). However, they all show variable enrichment of Re over Pd.

The Keluo mantle xenoliths do not show any correlation between $^{187}Re/^{188}Os$ and $^{187}Os/^{188}Os$ (Fig. 10a). Their $^{187}Re/^{188}Os$ ratios are highly variable ranging from 0.02 to 12.16, half of which are larger than the inferred values of the PUM (Meisel et al., 2001). The Keluo mantle xenoliths have heterogeneous Os isotope compositions, with $^{187}Os/^{188}Os$ ratios varying from 0.11458 to 0.13194. All samples but the harzburgite KL3-41 have $^{187}Os/^{188}Os$ ratios lower than the inferred values (0.1296 ± 6) of the PUM (Meisel et al., 2001). Their Re-depletion ages (T_{RD}) calculated relative to the PUM vary from 2.09 Ga to a modern age. However, only eight samples give a meaningful Re–Os isotope model age (T_{MA}) varying from 0.01 to 2.64 Ga. Other samples give T_{MA} either older than the age of the Earth or a future age, suggesting a disturbance of the Re–Os isotope system in these samples. Most Keluo mantle xenoliths show an approximate correlation between $^{187}Os/^{188}Os$ and bulk Al_2O_3 contents (Fig. 10b), whereas the dunites, together with two harzburgites, clearly deviate from this correlation.

5. Discussion

5.1. Melt depletion and metasomatic processes

The Keluo mantle xenoliths show different mineral modal contents, ranging from fertile lherzolite via clinopyroxene-poor

Table 2
Sr–Nd–Hf isotope compositions of clinopyroxene of the Keluo mantle xenoliths. The eruption age of the Keluo volcano is from (Liu, 1987). The Sm–Nd and Lu–Hf isotope composition of the CHUR: $^{147}Sm/^{144}Nd = 0.1967$, $^{143}Nd/^{144}Nd = 0.512638$; $^{176}Lu/^{177}Hf = 0.0332$, $^{176}Hf/^{177}Hf = 0.282772$. The Sm–Nd and Lu–Hf isotope compositions of the depleted mantle: $^{147}Sm/^{144}Nd = 0.2137$, $^{143}Nd/^{144}Nd = 0.513151$; $^{176}Lu/^{177}Hf = 0.0384$, $^{176}Hf/^{177}Hf = 0.28325$.

	t (Ma)	Rb (ppm)	Sr (ppm)	87Rb/86Sr	87Sr/86Sr	2σm	ISr	Sm (ppm)	Nd (ppm)	147Sm/144Nd	143Nd/144Nd	2σm	TDM (Ga)	εNd(t)	Lu (ppm)	Hf (ppm)	176Lu/177Hf	176Hf/177Hf	2σm	εHf(t)	TDM (Ga)
Standard																					
BCR-1					0.704977	0.000012					0.512655	0.000005						0.282866	0.000006		
BHVO-2					0.703474	0.000011					0.513000	0.000015						0.283109	0.000005		
Sample																					
KL-3-24	0.13	1.23	213.9	0.017	0.706267	0.000012	0.7063								0.167	2.464	0.0097	0.282839	0.000009	2.4	0.76
KL-3-26	0.13	0.40	68.9	0.017	0.704394	0.000013	0.7044	2.614	8.310	0.1902	0.512792	0.000012	2.31	2.80	0.110	0.560	0.0279	0.283255	0.000027	17.1	−0.03
KL3-27-1	0.13	0.20	55.4	0.011	0.703776	0.000013	0.7038	2.994	10.36	0.1747	0.512683	0.000011	1.82	0.66	0.087	0.975	0.0127	0.282919	0.000008	5.2	0.69
KL3-27-2	0.13	0.24	64.6	0.011	0.703809	0.000014	0.7038								0.123	1.373	0.0128	0.282913	0.000008	5.0	0.70
KL3-28	0.13	0.19	61.3	0.009	0.704228	0.000012	0.7042	2.236	7.177	0.1884	0.512912	0.000013	1.43	5.18	0.169	0.621	0.0388	0.283369	0.000020	21.1	14.65
KL3-30	0.13	0.27	124.7	0.006	0.705298	0.000013	0.7053								0.069	0.806	0.0121	0.282882	0.000019	3.9	0.74
KL3-38	0.13	0.20	82.2	0.007	0.704969	0.000013	0.7050	2.237	8.256	0.1638	0.512775	0.000014	1.15	2.50	0.090	0.505	0.0254	0.283256	0.000014	17.1	−0.03
08KL-01	0.13	0.07	63.2	0.003	0.704574	0.000017	0.7046	2.029	6.874	0.1785	0.512799	0.000007	1.52	2.99	0.165	0.761	0.0308	0.283183	0.000025	14.5	0.47
08KL-03	0.13	0.12	56.0	0.006	0.703635	0.000010	0.7036	2.626	7.762	0.2046	0.512888	0.000008	4.35	4.68	0.259	1.066	0.0346	0.283287	0.000011	18.2	−0.52
08KL-04	0.13	0.18	49.5	0.011	0.704182	0.000011	0.7042	1.935	6.007	0.1948	0.512717	0.000009	3.47	1.39	0.217	1.019	0.0303	0.283155	0.000013	13.5	0.63
08KL-05	0.13	0.16	113.6	0.004	0.704334	0.000013	0.7043	1.681	6.189	0.1642	0.512990	0.000012	0.49	6.74	0.224	0.925	0.0344	0.283884	0.000014	39.3	−9.27
08KL-07	0.13	0.22	101.3	0.006	0.704570	0.000016	0.7046	4.222	19.04	0.1341	0.512855	0.000014	0.57	3.91	0.103	1.304	0.0112	0.283027	0.000010	9.0	0.44
08KL-09	0.13	3.17	77.7	0.118	0.704416	0.000013	0.7044	1.983	6.647	0.1804	0.512643	0.000011	2.31	−0.05	0.243	1.242	0.0278	0.283173	0.000009	14.2	0.39
08KL-10	0.13	0.10	67.2	0.004	0.704963	0.000008	0.7050	1.686	4.840	0.2107	0.513033	0.000010	5.91	7.58	0.269	0.891	0.0428	0.283286	0.000012	18.2	0.43
08KL-11	0.13	0.20	329.2	0.002	0.704538	0.000008	0.7045	8.882	42.22	0.1272	0.512684	0.000006	0.82	0.22	0.100	5.933	0.0024	0.282882	0.000004	3.9	0.54
08KL-12	0.13	0.27	75.2	0.010	0.704791	0.000010	0.7048	2.208	7.639	0.1748	0.512796	0.000010	1.39	2.92	0.187	0.875	0.0304	0.283162	0.000015	13.8	0.59
08KL-13	0.13	0.83	154.8	0.016	0.704960	0.000011	0.7050	3.133	12.15	0.1559	0.512664	0.000009	1.28	0.27	0.155	2.342	0.0094	0.282548	0.000010	−7.9	1.28

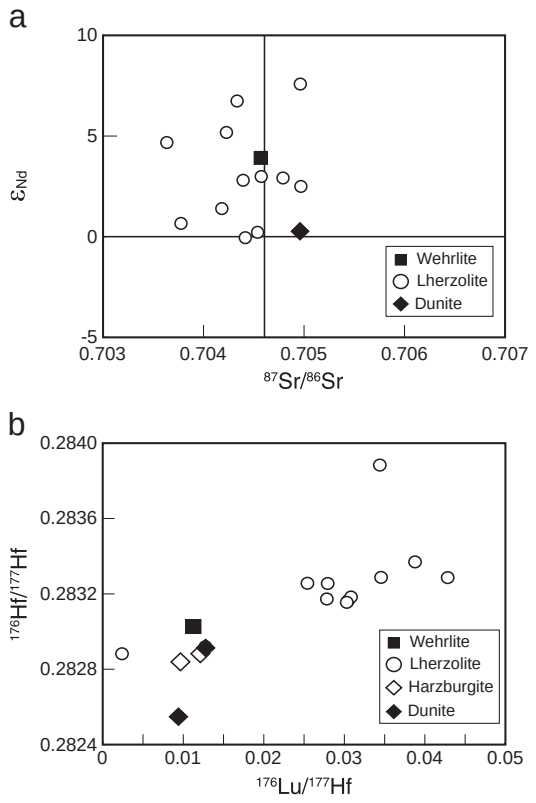

Fig. 8. Diagrams of $^{87}Sr/^{86}Sr$ vs. ε_{Nd} (a) and $^{176}Lu/^{177}Hf$ vs. $^{176}Hf/^{177}Hf$ (b) of clinopyroxene of Keluo mantle xenoliths.

lherzolites to strongly refractory harzburgites. Such a modal variation is accompanied by changes in mineral and bulk-rock chemical compositions. This indicates that the Kelou peridotite xenoliths represent the refractory residues left after variable degrees of melt depletion. The degrees of partial melting experienced by the Kelou xenoliths can be estimated using the Y and Yb contents of clinopyroxene, as described by Norman (1998). Comparison of Y and Yb contents in clinopyroxene and the modeled melting trend give melting degrees of 1–5% for lherzolites and 3–11% for harzburgites and dunites (Fig. 11). However, degrees of partial melting of the Kelou mantle xenoliths might be underestimated, as most Kelou mantle xenoliths, in particular the harzburgites and dunites, show characteristics of melt metasomatism. For example, both bulk-rock and clinopyroxene of most Keluo mantle xenoliths show variable enrichment in incompatible elements (Figs. 5 and 6). Furthermore, olivine in the dunite (KL3-27-2) has a Fo content lower than those in most lherzolites and harzburgites. Dunites with low-Fo olivines could be produced by reaction with basaltic melts (Morgan and Liang, 2005), which has been proposed for the discordant dunite bodies in ophiolites (Kelemen, 1990; Suhr, 1999). These characteristics are clearly not related to melt depletion, but are due to the interaction of the xenoliths with metasomatic melts.

The metasomatic agents proposed to account for the observed incompatible element features and mineralogy in mantle xenoliths include silicate melts (Zangana et al., 1999), hydrous (Downes, 2001) or CO_2-rich fluids (O'Reilly and Griffin, 1988), and carbonatitic melts (Coltorti et al., 1999; Ionov et al., 1997; Rudnick et al., 1993; Yaxley et al., 1998). Occurrence of phlogopite and rutile in two samples indicates modal metasomatism by hydrous melts in these samples, whereas absence of secondary minerals in most samples supports the cryptic metasomatism responsible for the enrichment of the incompatible elements. It has been suggested that mantle xenoliths metasomatized by carbonatite melts would be more enriched LREE but depleted in HFSEs (e.g., Ti and Zr) than by silicate melts (Coltorti

Table 3
Highly siderophile element (HSE) and Re–Os isotope compositions of the Keluo mantle xenoliths. The parameters used in the calculation are: $\lambda = 1.666\times10^{-11}$, $(^{187}Re/^{188}Os)_{PUM} = 0.42$, $(^{187}Os/^{188}Os)_{PUM} = 0.1296$. The chondritic normalization data are from McDonough and Sun (1995).

	t Ma	T (BK) oC	Fo	Al2O3 (wt%)	Os (ppb)	Ir (ppb)	Ru (ppb)	Pt (ppb)	Pd (ppb)	Re (ppb)	187Re/188Os	187Os/188Os	2σm	γOs	(187Os/188Os)i	TRD (Ga)	TMA (Ga)
Standard																	
WPR-1					16.7	14.2	22.3	289	238	10.9		0.14482	0.00002				
Sample																	
KL3-24	0.13	855	91.7	1.28	0.73					0.055	0.36	0.11807	0.00008	−8.9	0.11807	1.61	10.62
KL3-26	0.13	853	90.7	2.66	0.58					0.067	0.55	0.12434	0.00029	−4.1	0.12434	0.74	−2.49
KL3-27-1	0.13	781	90.7	2.69	0.65					0.475	3.51	0.12848	0.00089	−0.9	0.12848	0.16	−0.02
KL3-27-2	0.13	686	88.5	0.73	0.81					0.018	0.10	0.12981	0.00018	0.2	0.12981	−0.03	−0.04
KL3-28	0.13	835	90.2	3.31	2.55					0.067	0.13	0.12457	0.00045	−3.9	0.12457	0.71	1.01
KL3-30	0.13	902	90.8	0.74	0.72					0.079	0.52	0.12333	0.00007	−4.8	0.12333	0.88	−3.83
KL3-31	0.13	950	90.8	2.70	0.59					0.084	0.68	0.12209	0.00013	−5.8	0.12209	1.05	−1.78
KL3-38	0.13	872	90.6	1.74	0.54					0.040	0.35	0.12162	0.00026	−6.2	0.12162	1.12	6.52
KL3-40	0.13	869	91.4	0.77	0.60					0.002	0.02	0.11458	0.00010	−11.6	0.11458	2.09	2.17
KL3-41	0.13	860	91.0	1.35	0.28					0.702	12.16	0.13194	0.00021	1.8	0.13191	−0.33	0.01
08KL-01	0.13	832	89.5	1.93	1.60	1.45	2.78	5.56	2.50	0.925	2.78	0.12172	0.00020	−6.1	0.12171	1.11	−0.20
08KL-02	0.13	1016	90.8	0.94	2.48	1.80	4.21	3.17	0.50	0.056	0.11	0.11602	0.00011	−10.5	0.11602	1.89	2.54
08KL-03	0.13	1070	89.0	3.48	1.46	1.56	2.49	4.72	1.79	0.196	0.65	0.12531	0.00007	−3.3	0.12531	0.60	−1.17
08KL-04	0.13	880	89.3	2.95	1.40	1.52	2.73	3.73	1.22	0.058	0.20	0.11949	0.00010	−7.8	0.11949	1.42	2.64
08KL-05	0.13	842	89.1	1.95	3.79	1.78	4.13	3.74	1.86	0.026	0.03	0.12049	0.00014	−7.0	0.12049	1.28	1.38
08KL-07	0.13	551	90.6	1.82	1.48	0.83	1.57	2.22	0.95	0.526	1.71	0.11593	0.00068	−10.5	0.11593	1.91	−0.64
08KL-09	0.13	797	88.1	3.99	1.42	1.34	2.30	4.23	1.97	0.183	0.62	0.12759	0.00012	−1.6	0.12759	0.28	−0.62
08KL-10	0.13	888	88.7	3.50	0.74	0.96	1.92	3.34	1.32	0.234	1.53	0.12682	0.00021	−2.1	0.12682	0.39	−0.15
08KL-11	0.13	927	90.7	1.57	1.71	1.66	1.92	3.34	0.69	1.731	4.86	0.12226	0.00006	−5.7	0.12225	1.03	−0.10
08KL-12	0.13	774	89.4	1.83	1.63	1.81	3.42	9.35	6.84	0.027	0.08	0.12563	0.00060	−3.1	0.12563	0.56	0.69
08KL-13	0.13	849	90.3	0.65	1.50	1.45	2.40	1.81	0.23	0.019	0.06	0.12093	0.00019	−6.7	0.12093	1.22	1.42

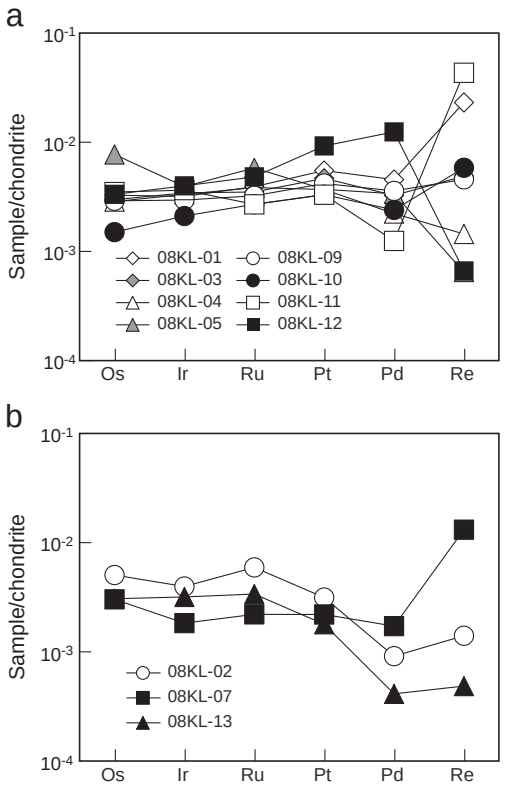

Fig. 9. Highly siderophile element patterns of (a) lherzolites and (b) harzburgite, dunite and wehrlite, normalized to the chondrite values of McDonough and Sun (1995).

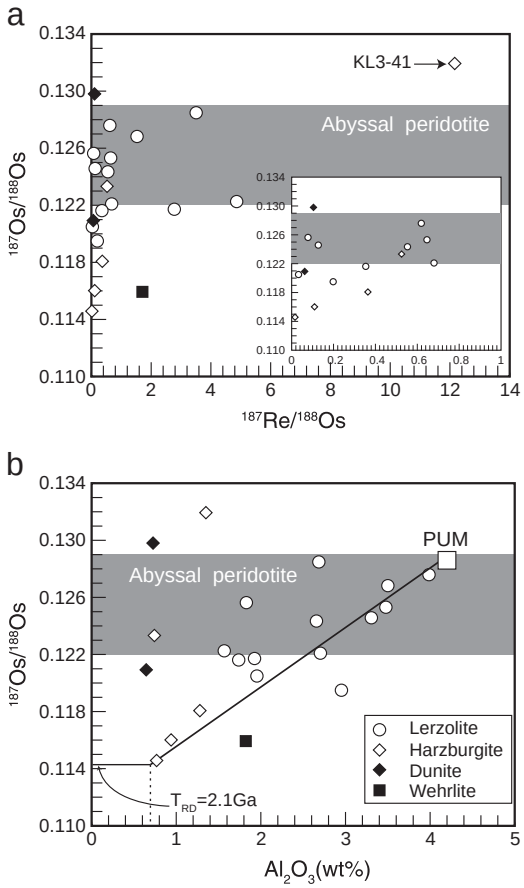

Fig. 10. Diagrams of $^{187}Os/^{188}Os$ ratios vs. $^{187}Re/^{188}Os$ ratios (a) and bulk Al_2O_3 contents (b) of Keluo mantle xenoliths. The abyssal peridotite data are from Snow and Reisberg (1995) and Brandon et al. (2000). PUM: primitive upper mantle (Meisel et al., 2001).

et al., 1999). Clinopyroxenes in the Kelou mantle xenoliths have low La/Yb but high Ti/Eu ratios, which are consistent with metasomatism by silicate melts rather than carbonatite melts (Fig. 12). However, the formation of wehrlite (08KL-07) and the elevated CaO/Al_2O_3 ratios in two samples (KL3-27-1 and 08KL-07) imply that the lithospheric mantle was locally modified by carbonatite melt.

5.2. Effect of secondary processes on Re–Os isotopes

After melt extraction and stabilization, the lithospheric mantle might also undergo various secondary processes, such as refertilization, melt metasomatism and sulfide breakdown, which have the potential to disturb Re–Os isotope systematics. As discussed above, the Keluo mantle xenoliths have been partially metasomatized by silicate melts and probably carbonatite melts. Although it has been suggested that Os isotopes of mantle peridotites can survive secondary processes and provide robust age information (Rudnick and Walker, 2009), the effects of these metasomatic processes should be evaluated before we use the Re–Os isotopes to constrain the age of the lithospheric mantle.

Most of the Keluo mantle xenoliths that have been analyzed for HSE compositions show enrichment in Re over Pd (Fig. 9), and Re contents of some xenoliths are higher than the PUM (0.34 ± 6 ppb; Meisel et al., 2001). This implies the addition of Re to these samples during metasomatism. High Re contents also result in high $^{187}Re/^{188}Os$ ratios in these samples; in particular, sample KL3-41 that has a $^{187}Re/^{188}Os$ ratio up to 12. However, it should be noted that several samples with low Re contents also have high $^{187}Re/^{188}Os$ ratios. For example, sample KL3-26 contains 0.067 ppb Re, which is much lower the PUM, but has $^{187}Re/^{188}Os$ ratio (0.55) higher than the PUM (0.43; Meisel et al., 2001). This might be ascribed to the low Os contents of the Keluo mantle xenoliths, especially for the KL-series samples. Most of the KL-series xenoliths have Os contents less than 1 ppb, which is considerably lower than the 08KL-series samples (Table 3). The reason for this is not clear, as there is no obvious difference in textures and compositions between samples from these two series.

It has been demonstrated that some mantle xenoliths commonly have Os contents lower than those of the compositionally similar massif and abyssal peridotites, and this has been attributed to sulfide breakdown (Handler et al., 1999; Liu et al., 2010b). Sulfide breakdown

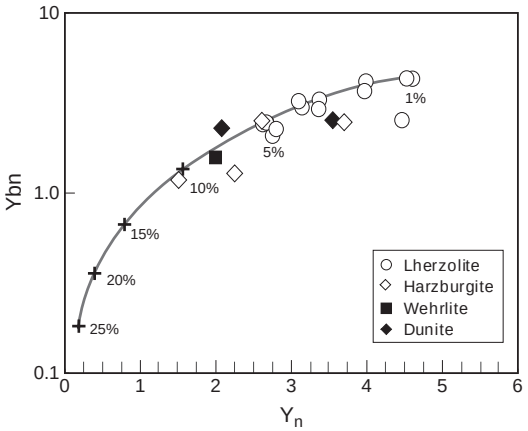

Fig. 11. A comparison of fractional melting model with the Y and Yb contents of clinopyroxene from the Keluo mantle xenoliths. The fractional melting model is modified after Norman (1998). n: primitive mantle normalized (McDonough and Sun, 1995).

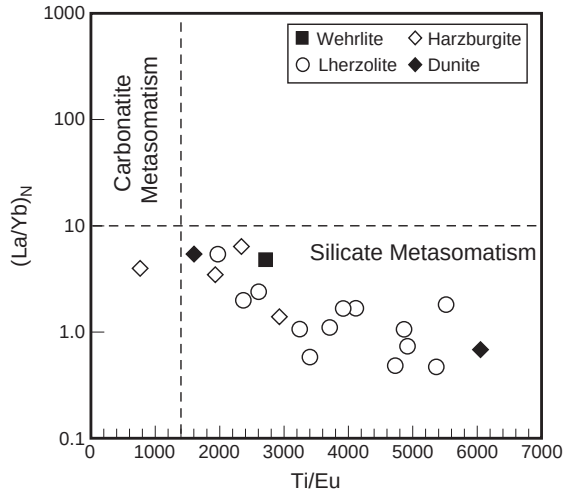

Fig. 12. Diagram of $(La/Yb)_n$ vs. Ti/Eu ratios of clinopyroxenes in the Kelou mantle xenoliths. Areas of carbonatite and silicate metasomatism are from Coltorti et al. (1999).

is a common phenomenon in many peridotitic mantle xenoliths and may be related to percolation of sulfur-undersaturated melts associated with the host volcanism (Reisberg et al., 2005) or post-eruption oxidative weathering (Handler et al., 1999). It has been suggested that sulfide breakdown occurred immediately prior to, or coincident with the entrainment of the xenoliths in the host lava has negligible effect on the Os isotope compositions (Rudnick and Walker, 2009).

Melt-rock reaction is another way possible to reduce the Os contents of mantle peridotites. At high melt/rock ratios, the undersaturated melts tend to scavenge the primary unradiogenic Os from the mantle peridotites, resulting in the significant decrease in Os concentrations (Büchl et al., 2002). In this case, the secondary sulfides subsequently precipitated from the later melts will dominate the Os isotope compositions of the 'reactive' peridotites. Precipitation of secondary sulfides would add radiogenic Os to the reactive harzburgites and dunites, resulting in radiogenic $^{187}Os/^{188}Os$ ratios (Büchl et al., 2002). Low-Fo contents of olivine in the dunite KL3-27-2 support its reactive origin. Its low Os concentration (0.81 ppb) reflects the significant removal of the primary Os, whereas its radiogenic $^{187}Os/^{188}Os$ (0.12981) but low $^{187}Re/^{188}Os$ ratios indicate the addition of radiogenic Os into this sample. The harzburgite KL3-41 with an even lower Os content (0.28 ppb) should be even more sensitive to the addition of secondary Os, as reflected by its $^{187}Os/^{188}Os$ ratio (0.13191), which is more radiogenic than the inferred values (0.1296 ± 8) of the PUM (Meisel et al., 2001).

5.3. Age of the SCLM beneath eastern CAOB

There are various methods that can be used to constrain ages of peridotites using the Re–Os system, including T_{MA} model age, Re-depletion age (T_{RD}) and proxy-isochron age. The T_{MA} model age used the sample's measured Re/Os ratio to calculate the time of its separation from the PUM reservoir. It may yield unreliable model ages if Re has been removed or added into peridotites. Thirteen Keluo mantle xenoliths yield impossible T_{MA} model ages, i.e., negative or greater than the Earth's age, reflecting the modification of Re/Os ratios shortly before, during or since basalt entrainment. This is obvious for sample KL3-41, which has an $^{187}Re/^{188}Os$ ratio (>12) significantly higher than that of the PUM (0.43).

However, recent Re addition does not strongly affect the $^{187}Os/^{188}Os$ ratio, because the time is too short for decay increase. Therefore, recent addition of Re into mantle peridotites has little effect on T_{RD}, which assumes no Re is left in the residual mantle peridotites after melt extraction. Samples KL3-27-2 and KL3-41, both with obvious Os addition, give unreliable T_{RD}. Other Keluo xenoliths give T_{RD} (calculated relative to the PUM) varying from 2.1 to 0.16 Ga. It should be noted that the T_{RD} age underestimates the true age of melting because of the incomplete removal of Re, and represents the minimum age of melt extraction (Walker et al., 1989). This is especially significant for lherzolites, which commonly experience low degrees of melting and retain abundant Re after melt extraction. Only the refractory harzburgites with little residual Re can give a T_{RD} age that approach the true age of melting. Two refractory harzburgites KL3-40 and 08KL-02 with low Al_2O_3 contents (0.77 wt.% and 0.94 wt.%, respectively) have very unradiogenic $^{187}Os/^{188}Os$ ratios, giving the oldest T_{RD} ages of 1.9–2.1 Ga. A previous Re–Os isotope study on sulfides in mantle xenoliths from the Xing-Meng Block have reported that the T_{RD} are dominated by Neoproterozoic to Mesozoic ages, with minor Paleoproterozoic to Mesoproterozoic ages (Xu et al., 2008).

The proxy-isochron age has been commonly applied to determine the model age of peridotites that are assumed to have a common origin through melt extraction, in which the $^{187}Os/^{188}Os$ is plotted against an immobile element that has a similar bulk partition coefficient to Re during melting. Such elements include aluminum, heavy rare earth elements (HREE) or yttrium (Peslier et al., 2000b; Reisberg and Lorand, 1995). In the Al_2O_3-$^{187}Os/^{188}Os$ plot (Fig. 10b), the Keluo mantle xenoliths show a highly scattered but positive trend among the lherzolites and three refractory harzburgites. It has been argued that about 0.7% Al_2O_3 is left after Re is totally extracted from the mantle peridotites (Handler and Bennett, 1999). Extrapolation of the alumochron of the Keluo xenoliths to 0.7% Al_2O_3 corresponds to an $^{187}Os/^{188}Os$ ratio of ~0.114, giving a T_{RD} age of 2.1 Ga. This agrees well with the T_{RD} of the most refractory harzburgites. Therefore, the Re–Os isotopes constrain that the SCLM beneath the Keluo area was probably formed during the Paleoproterozoic.

Previous studies on abyssal peridotites have demonstrated that the asthenospheric mantle is highly heterogeneous in Os isotopes (Brandon et al., 2000; Harvey et al., 2006; Liu et al., 2008; Pearson et al., 2007; Snow and Reisberg, 1995), in which some ancient domains with ages up to 2 Ga can be preserved from the convecting homogenization processes of the asthenosphere (Liu et al., 2008). Therefore, the ancient Os model ages of some Keluo mantle xenoliths might reflect the ancient mantle domains in the asthenosphere. In this case, the SCLM beneath the eastern part of Central Asian Orogenic Belt (CAOB) could be juvenile oceanic mantle with an ancient mantle 'blob' of the Paleoproterozoic age preserved. A similar mechanism has been proposed to account for the Re–Os isotope composition of the Cenozoic mantle xenoliths from both eastern NCC and NE China (Chu et al., 2009; Zhou et al., 2007, 2010).

Nevertheless, the following evidence does not favor the existence of SCLM beneath eastern CAOB representing young mantle accreted from asthenosphere. Firstly, the Keluo mantle xenoliths show pervasive metasomatism by K-rich fluids/melts and contain abundant phlogopite, which only rarely occurs in the mantle xenoliths from eastern NCC and northeastern China. Furthermore, clinopyroxene in Keluo xenoliths have Sr–Nd–Hf isotope compositions distinct from mantle xenoliths from both eastern NCC and northeastern China. In the Sr–Nd isotope diagram, the Keluo mantle xenoliths plot near the enriched end-member of the Cenozoic mantle xenoliths from eastern NCC and northeastern China (Fig. 13a). The difference is clearer in the Nd–Hf isotope diagram (Fig. 13b), in which most Keluo mantle xenoliths plot outside the area defined by mantle xenoliths from the eastern NCC and northeastern China. Finally, it has been concluded that potassic basalts in the WEK area were derived from an old EM1-type lithospheric mantle that was metasomatized at ca. 1.9 Ga (Zhang et al., 1995, 1998). Both Nd and Hf isotopes of clinopyroxene from the Keluo mantle xenoliths also give ancient model ages, reflecting the old metasomatic events in the SCLM (Table 2).

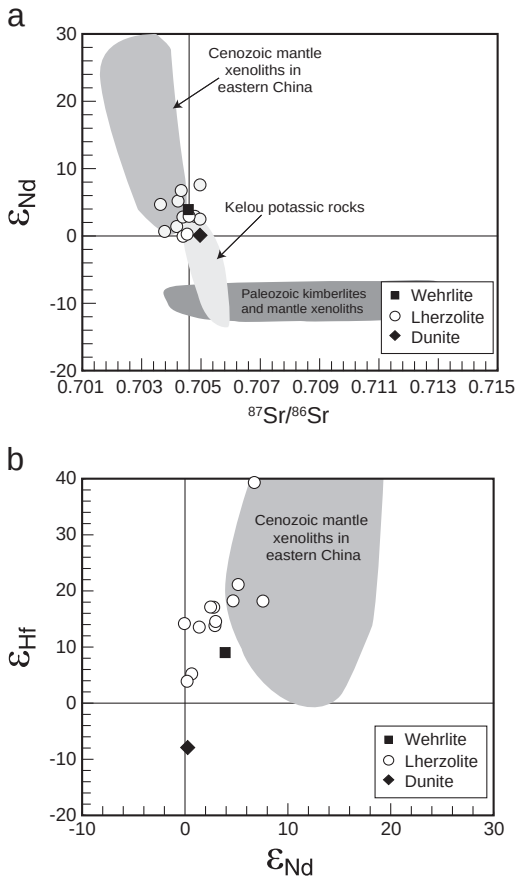

Fig. 13. Diagrams of ε_{Nd} vs. $^{87}Sr/^{86}Sr$ (a) and ε_{Hf} (b) of clinopyroxene of Keluo mantle xenoliths. Data of the Cenozoic mantle xenoliths from eastern China are from (Chu et al., 2009; Liu et al., 2010c; Wu et al., 2006; Zhou et al., 2007, 2010), the Paleozoic kimberlites and mantle xenoliths are from (Chi and Lu, 1996; Fan et al., 2000; Zheng, 1999), and Keluo potassic rocks are from (Basu et al., 1991; Mu et al., 1992; Zhang et al., 1995, 1998; Zou et al., 2000).

5.4. Crust–mantle decoupling in eastern CAOB

As the residues formed after the extraction of continental crust, the sub-continental lithospheric mantle (SCLM) is commonly coupled, both mechanically and temporally, with the overlying crust (Carlson et al., 2005; Pearson, 1999). However, the cratonic SCLM is not always temporally coupled with the overlying crust. It has been demonstrated that the old SCLM in some cratons (e.g., Slave and Wyoming cratons) has been partly removed and replaced by young mantle (Aulbach et al., 2004; Carlson et al., 1999; Griffin et al., 1999), which resulted in a temporally and compositionally layered lithospheric mantle. The North China Craton (NCC) provides the best case for removal of old lithospheric mantle, in which the Archean lithospheric mantle beneath the eastern NCC has been significantly removed (Gao et al., 2002; Griffin et al., 1998; Menzies et al., 1993; Wu et al., 2003b; Xu, 2001).

In contrast to the eastern NCC, a reverse crust–mantle temporal structure is shown in the lithosphere beneath eastern part of the Central Asian Orogenic Belt (CAOB; Fig. 14). The Re–Os isotopes of mantle xenoliths reveal the existence of the Paleoproterozoic SCLM beneath the CAOB during the Cenozoic. Furthermore, it has been suggested that potassic basalts in the WEK areas were derived from an ancient lithospheric mantle as old as the Paleoproterozoic i.e., ca. 1.9 Ga (Zhang et al., 1995, 1998). Nevertheless, previous studies on both granites and felsic volcanic rocks have suggested that the crustal growth in the CAOB was predominately occurred since the Neoproterozoic, with a little in Mesoproterozic (Ge et al., 2007; Hong et al., 2000; Jahn et al., 2000, 2004; Sui et al., 2007; Wu et al., 2000, 2002, 2003a; Zhang et al., 2010). A previous study on zircons from Longzheng granites in the Keluo area has obtained that positive $\varepsilon_{Hf}(t)$ values of +6–+13 and model ages of 511–958 Ma (Zhang et al., 2010). Therefore, the SCLM beneath the Keluo area is older than expected based on crustal age determinations.

The temporal decoupling implies there is no direct genetic link between the mantle and the crustal basement in eastern CAOB. A possibility is that the old lithospheric mantle is exotic, which was transported from elsewhere and impinged beneath the Keluo area. For example, it has been suggested that the enriched lithospheric mantle beneath the western Yangtze Craton, which is responsible for the ultrapotassic rocks along the northern Ailao Shan-Red River Fault, was extruded from the Tibetau plateau (Xu et al., 2001). Furthermore, Wu et al. (2006) suggested that the Cenozoic mantle xenoliths with Paleoproterozoic ages represent old mantle beneath the NE China, which was probably extruded from the Yangtze Craton due to the Triassic collision between North China and South China. Another possible scenario is that younger crust was late tectonically accreted to the older mantle in the eastern part of the CAOB. Similar mechanisms have been proposed to explain the crust–mantle decoupling Canadian Cordillera (Peslier et al., 2000a, 2000b). This model raises the question as to why the lithospheric mantle was stable through the complicated orogenic activities in eastern CAOB since the Phanerozoic, during which the Paleo-Asian and Paleo-Pacific Ocean were sequentially subducted.

6. Conclusion

Mantle xenoliths entrained in the Cenozoic Keluo potassic rocks show complicated histories of melting and metasomatism. They have been mainly metasomatized by silicate melts and locally by K-rich hydrous melts. Although the Re–Os isotope system has been disturbed, the Os isotope compositions of most Kelou mantle xenoliths have not been significantly modified by metasomatic

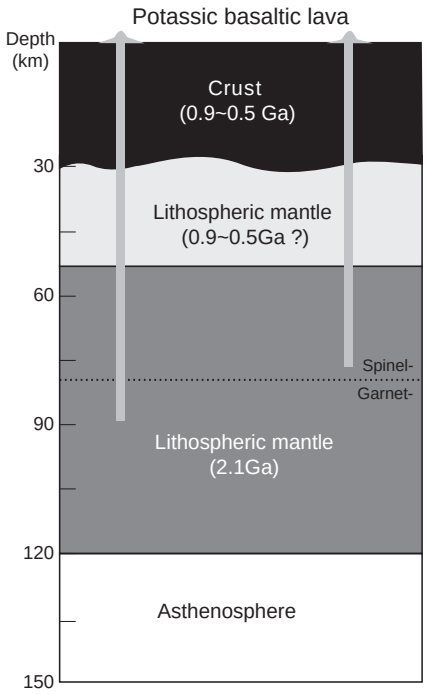

Fig. 14. Inferred lithospheric structure beneath the Kelou area. The crust in the Kelou area was mainly formed since the Neoproterozoic. The underlain lithospheric mantle might have similar ages with the overlying crust. Lithospheric mantle with an ancient age of ca. 2.1 Ga drifted from elsewhere and was accreted beneath the Kelou area, which became the mantle source of the potassic basaltic lavas.

processes. Both T_{RD} ages of the refractory harzburgites and the alumochron age, constrain the formation of the sub-continental lithospheric mantle beneath the Keluo at about 2.1 Ga. This is in contrast to the younger model ages of the overlying crust. The old mantle underlying this region does not represent the ancient mantle preserved in the asthenosphere. Thus, the crust and mantle are temporally decoupled in the eastern part of the Central Asian Orogenic Belt (CAOB). The old mantle could be exotic and was extruded from elsewhere, e.g., from the Yangtze Craton due to the collision between North China and South China.

Supplementary materials related to this article can be found online at doi:10.1016/j.lithos.2011.07.022.

Acknowledgment

This work was financially supported by the by the National Natural Science Foundation of China (No. 90814003) and Graduate Innovation Fund of Jilin University (No. 20111038). We thank Yu-Guang Ma, Qian Mao, Lie-Wen Xie, Yue-Heng Yang, Yan-Bin Zhang, Jin-Feng Sun, Zhi-Chao Liu, Qin Zhou, Jing Sun and Ji-Heng Zhang at the IGGCAS, Yin Liu and Xiang-Lin Tu at GIGCAS, for help in analysis. Reviews by Sue O'Reilly and other anonymous reviewers significantly improved the quality of this paper.

References

Aulbach, S., Griffin, W.L., Pearson, N.J., O'Reilly, S.Y., Kivi, K., Doyle, B.J., 2004. Mantle formation and evolution, Slave Craton: constraints from HSE abundances and Re–Os isotope systematics of sulfide inclusions in mantle xenocrysts. Chemical Geology 208, 61–88.

Basu, A.R., Wang, J.W., Hang, W.K., Xie, G.H., Tatsumato, M., 1991. Major element, REE and Pb, Nd and Sr isotopic geochemistry of Cenozoic volcanic rocks of eastern China: implications of their origin form suboceanic-type mantle reservoirs. Earth and Planetary Science Letters 105, 149–469.

Becker, H., Horan, M.F., Walker, R.J., Gao, S., Lorand, J.P., Rudnick, R.L., 2006. Highly siderophile element composition of the Earth's primitive upper mantle: Constraints from new data on peridotite massifs and xenoliths. Geochimica et Cosmochimica Acta 70, 4528–4550.

Birck, J.L., Roy-Barman, M., Capmas, F., 1997. Re–Os isotopic measurements at the femtomole level in natural samples. Geostandards Newsletter 21, 19–27.

Boyd, F.R., 1989. Compositional distinction between oceanic and cratonic lithosphere. Earth and Planetary Science Letters 96, 15–26.

Brandon, A.D., Snow, J.E., Walker, R.J., Morgan, J.W., Mock, T.D., 2000. ^{190}Pt-^{186}Os and ^{187}Re-^{187}Os systematics of abyssal peridotites. Earth and Planetary Science Letters 177, 319–335.

Büchl, A., Brügmann, G., Batamova, V.G., Münker, C., Hofmann, A.W., 2002. Melt percolation monitored by Os isotopes and HSE abundances: a case study from the mantle section of the Troodos ophiolite. Earth and Planetary Science Letters 204, 385–402.

Carlson, R.W., Irving, A.J., Hearn, J.B.C., 1999. Chemical and isotopic systematics of peridotites xenoliths from the Williams kimberlite, Montana: clues to processes of lithosphere formation, modification and destruction. In: Gurney, J.J., Gurney, J.L., Pescoe, M.D., Richardson, S.H. (Eds.), Proceedings of the seventh international kimberlite conference. Cape Town, South Africa, pp. 90–98.

Carlson, R.W., Pearson, D.G., James, D.E., 2005. Physical, chemical, and chronological characteristics of continental mantle. Reveiws of Geophysics 43, RG1001. doi:10.1029/2004rg000156.

Chi, J.S., Lu, F.X., 1996. Kimberlites and the features of Paleozoic lithospheric mantle in North China craton. Science Press, Beijing.

Chu, Z.Y., Wu, F.Y., Walker, R.J., Rudnick, R.L., Pitcher, L., Yang, Y.H., A.W.S., 2009. Temporal evolution of the lithospheric mantle beneath the eastern North China Craton. Journal of Petrology 50, 1857–1898.

Coltorti, M., Bonadiman, C., Hinton, R.W., Siena, F., Upton, B.G.J., 1999. Carbonatite metasomatism of the oceanic upper mantle: evidence from clinopyroxenes and glasses in ultramafic xenoliths of Grande Comore, Indian Ocean. Journal of Petrology 40, 133–165.

Downes, H., 2001. Formation and modification of the shallow sub-continental lithospheric mantle: a review of geochemical evidence from ultramafic xenoliths suites and tectonically emplaced ultramafic massifs of western and central Europe. Journal of Petrology 42, 233–250.

Fan, Q.C., Hooper, P.R., 1989. The mineral chemistry of ultramafic xenoliths of eastern China: Implications for upper mantle composition and the paleogeotherms. Journal of Petrology 30, 1117–1158.

Fan, W.M., Zhang, H.F., Baker, J., Jarvis, K.E., Mason, P.R.D., Menzies, M.A., 2000. On and off the North China Craton: where is the Archaean Keel? Journal of Petrology 41, 933–950.

Gao, S., Rudnick, R.L., Carlson, R.W., McDonough, W.F., Liu, Y.S., 2002. Re–Os evidence for replacement of ancient mantle lithosphere beneath the North China craton. Earth and Planetary Science Letters 198, 307–322.

Ge, W.C., Sui, Z.M., Wu, F.Y., Zhang, J.H., Xu, X.C., Cheng, R.Y., 2007. Zircon U–Pb ages, Hf isotopic characteristics and their implications of the Early Paleozoic granites in the northeastern Da Hinggan Mts, northeastern China. Acta Petrologica Sinica 23, 423–440.

Griffin, W.L., Zhang, A.D., O'Reily, S.Y., Ryan, C.G., 1998. Phanerozoic evolution of the lithosphere beneath the Sino-Korean craton. In: Flower, M.F.J., Chung, S.L., Lo, C.H., Lee, T.Y. (Eds.), Mantle Dynamics and Plate Interactions in East Asia, Geodynamic Series: American Geophysical Union, 27, pp. 107–126. Washington D.C.

Griffin, W.L., Doyle, B.J., Ryan, C.G., Pearson, N.J., O'Reilly, S.Y., Davies, R., Kivi, K., van Achterbergh, E., Natapov, L.M., 1999. Layered mantle lithosphere in the Lac de Gras area, Slave craton: Composition, structure and origin. Journal of Petrology 40, 705–727.

Griffin, W.L., Powell, W.J., Pearson, N.J., O'Reilly, S.Y., 2008. GLITTER: data reduction software for laser ablation ICP-MS. In: Sylvester, P. (Ed.), Laser Ablation-ICP-MS in the Earth Sciences: Mineralogical Association of Canada Short Course Series, vol. 40, pp. 204–207.

Guo, F., Fan, W.M., Li, C.W., Gao, X.F., Miao, L.F., 2009. Early Cretaceous highly positive εNd(t) felsic volcanic rocks from the Hinggan Mountains, NE China: origin and implications for Phanerozoic crustal growth. International Journal of Earth Sciences 98, 1395–1411.

Handler, M.R., Bennett, V.C., 1999. Behaviour of Platinum-group elements in the subcontinental mantle of eastern Australia during variable metasomatism and melt depletion. Geochimica et Cosmochimica Acta 63, 3597–3618.

Handler, M.R., Bennett, V.C., Dreibus, G., 1999. Evidence from correlated Ir/Os and Cu/S for late-stage Os mobility in peridotite xenoliths: implications for Re–Os systematics. Geology 27, 75–78.

Harvey, J., Gannoun, A., Burton, K.W., Rogers, N.W., Alard, O., Parkinson, I.J., 2006. Ancient melt extraction from the oceanic upper mantle revealed by Re–Os isotopes in abyssal peridotites from the Mid-Atlantic ridge. Earth and Planetary Science Letters 244, 606–621.

Herrmann, W., Berry, R.F., 2002. MINSQ-a least squares spreadsheet method for calculating mineral proportions from whole rock major element analyses. Geochemistry: Exploration, Environment, Analysis 2, 361–368.

Hong, D.W., Wang, S.G., Xie, X.L., Zhang, J.S., 2000. Genesis of positive εNd(t) granitoids in the Da Hinggan MTS.-Mongolia Oragenic Belt and growth continental crust. Earth Science Frontiers 7, 441–456 (in Chinese with English abstract).

Ionov, D.A., Griffin, W.L., O'Reilly, S.Y., 1997. Volatile-bearing minerals and lithophile trace elements in the upper mantle. Chemical Geology 141, 153–184.

Jahn, B.M., Wu, F.Y., Chen, B., 2000. Massive granitoids generation in central Asia: Nd isotopic evidence and implication for continental growth in the Phanerozoic. Episodes 23, 82–92.

Jahn, B.M., Capdevila, R., Liu, D.Y., Vernon, A., Badarch, G., 2004. Sources of Phanerozoic granitoids in the transect Bayanhongor-Ulaan Baatar, Mongolia: geochemical and Nd isotopic evidence, and implications for Phanerozoic crustal growth. Journal of Asian Earth Sciences 23, 629–653.

Kelemen, P.B., 1990. Reaction between ultramafic rock and fractionating basaltic magma I. Phase relations, the origin of calc-alkaline magma series, and the formation of discordant dunite. Journal of Petrology 31, 51–98.

Li, X.H., Li, Z.X., Wingate, M.T.D., Chung, S.L., Liu, Y., Lin, G.C., Li, W.X., 2006. Geochemistry of the 755 Ma Mundine Well dyke swarm, northwestern Australia: part of a Neoprozerotoic mantle superplume beneath Rodinia? Precambrian Research 146, 1–15.

Liu, J.Q., 1987. Study on geochronology of the Cenozoic volcanic rocks in northeast China. Acta Petrologica Sinica 3, 21–31 (In chinese with English abstract).

Liu, R.X., 1992. The age and geochemistry of Cenozoic volcanic rock in China. Seismic Press, Beijing.

Liu, C.Z., Snow, J.E., Hellebrand, E., Brügmann, G., von der Handt, A., Büchl, A., Hofmann, A.W., 2008. Ancient, highly heterogeneous mantle beneath Gakkel ridge, Arctic Ocean. Nature 452, 311–316.

Liu, C.Z., Snow, J.E., Brugmann, G., Hellebrand, E., Hofmann, A.W., 2009. Non-chondritic HSE budget in Earth's upper mantle evidenced by abyssal peridotites from Gakkel ridge (Arctic Ocean). Earth and Planetary Science Letters 283, 122–132 (English).

Liu, C.Z., Wu, F.Y., Wilde, S.A., Yu, L.J., Li, J.L., 2010a. Anorthitic plagioclase and pargasitic amphibole in mantle peridotites from the Yungbwa ophiolite (southwestern Tibetan Plateau) formed by hydrous melt metasomatism. Lithos 114, 413–422.

Liu, J.G., Rudnick, R.L., Walker, R.J., Gao, S., Wu, F.Y., Piccoli, P.M., 2010b. Processes controlling highly siderophile element fractionations in xenolithic peridotites and their inflence on Os isotopes. Earth and Planetary Science Letters 297, 287–297.

Liu, Z.C., Wu, F.Y., Chu, Z.Y., Xu, X.S., 2010c. Isotopic compositions of the peridotitic xenoliths from the Nushan area, Anhui Province: constraints on the age of subcontinental lithospheric mantle beneath the East China. Acta Petroligica Sinica 26, 1217–1240 (in Chinese with English abstract).

McDonough, W.F., Sun, S.S., 1995. The composition of the Earth. Chemical Geology 120, 223–253.

Meisel, T., Walker, R.J., Irving, A.J., Lorand, J.P., 2001. Osmium isotopic compositions of mantle xenoliths: a global perspective. Geochimica et Cosmochimica Acta 65, 1311–1323.

Menzies, M.A., Fan, W.M., Zhang, M., 1993. Paleozoic and Cenozoic lithoprobes and the loss of >120 km of Archean lithosphere, Sino-Korean craton, China. In: Prichard, H.M., Harris, N.B.W., Neary, C.R. (Eds.), Magmatic Processes and Plate Tectonics: Geological Society of London, 76, pp. 71–81. London.

Morgan, Z., Liang, Y., 2005. An experimental study of the kinetics of lherzolite reactive dissolution with applications to melt channel formation. Contributions to Mineralogy and Petrology 2005, 369–385.

Mu, Z.G., Liu, C., Huang, B.L., Hou, G.T., Zheng, D.Q., Cui, J.W., Liu, S.J., 1992. K–Ar ages and Geochemistry of the Late-Cenozoic volcanic rocks in Keluo, Heilongjiang province. Acta Scientiarum Naturalium Universitatis Pekenensis 28, 733–744 (in Chinese).

Norman, M.D., 1998. Melting and metasomatism in the continental lithosphere: laser ablation ICPMS analysis of minerals in spinel lherzolites from eastern Australia. Contributions to Mineralogy and Petrology 130, 240–255.
O'Reilly, S.Y., Griffin, W.L., 1988. Mantle metasomatism beneath western Victoria, Australia: I. Metasomatic processes in Cr-diopside lherzolites. Geochimica et Cosmochimica Acta 52, 433–447.
Pearce, N.J.G., Perkins, W.T., Westgate, J.A., Gorton, M.P., Jackson, S.E., Neal, C.R., Chenery, S.P., 1997. A compilation of new and published major and trace element data for NIST SRM 610 and NIST SRM 612 glass reference materials. Geostandards Newsletter 21, 115–144.
Pearson, D.G., 1999. The age of continental roots. Lithos 48, 171–194.
Pearson, D.G., Parman, S.W., Nowell, G.M., 2007. A link between large mantle melting events and continent growth seen in osmium isotopes. Nature 449, 202–205.
Peslier, A.H., Reisberg, L., Ludden, J., Francis, D., 2000a. Os isotopic systematics in mantle xenoliths; age constraints on the Canadian Cordillera lithosphere. Chemical Geology 166, 85–101.
Peslier, A.H., Reisberg, L., Ludden, L., Francis, D., 2000b. Re–Os constraints on harzburgite and iherzolite formation in the lithospheric mantle: a study of Nrothern Canadian Cordilliera xinoliths. Geochimica et Cosmochimica Acta 64, 3061–3071.
Reisberg, L., Lorand, J.P., 1995. Longevity of sub-continental mantle lithosphere from osmium isotope systematics in orogenic peridotite massifs. Nature 376, 159.
Reisberg, L., Zhi, X.C., Lorand, J.P., Wagner, C., Peng, Z.C., Zimmermann, C., 2005. Re–Os and S systematics of spinel peridotite xenoliths from east central China: evidence for contrasting effects of melt percolation. Earth and Planetary Science Letters 239, 286–308.
Rudnick, R.L., Walker, R.J., 2009. Interpreting ages from Re–Os isotopes in peridotites. Lithos 112, 1083–1095.
Rudnick, R.L., McDonough, W.F., Chappell, B.W., 1993. Carbonatite metasomatism in the northern Tanzanian mantle: petrographic and geochemical characteristics. Earth and Planetary Science Letters 114, 463–475.
Sengör, A.M.C., Natal'in, B.A., Burtman, V.S., 1993. Evolution of the Altaid tectonic collage and Palaeozoic crustal growth in Eurasia. Nature 364, 299–307.
Snow, J.E., Reisberg, L., 1995. Os isotopic systematics of the MORB mantle: results from altered abyssal peridotites. Earth and Planetary Science Letters 133, 411.
Suhr, G., 1999. Melt migration under oceanic ridges: inferences from reactive transport modelling of upper mantle hosted dunites. Journal of Petrology 40, 575–599.
Sui, Z.M., Ge, W.C., Wu, F.Y., Zhang, J.H., Xu, X.C., Cheng, R.Y., 2007. Zircon U–Pb ages, geochemistry and its petrogenesis of Jurassic granites in northeastern part of the Da Hinggan Mountains. Acta Petrologica Sinica 23, 461–480 (in Chinese with English abstract).
Sun, S.S., McDonough, W.F., 1989. Chemical and isotopic systematics of oceanic basalts: implications for mantle composition and processes. In: Saunder, A.D., Norry, M.J. (Eds.), Magmatism in the Ocean Basin: Special Publication of the Geological Society of London, 42, pp. 313–346.
Walker, R.J., Carlson, R.W., Shirey, S.B., Boyd, F.R., 1989. Os, Sr, Nd, and Pb isotope systematics of Southern African peridotite xenoliths: implications for the chemical evolution of subcontinental mantle. Geochimica et Cosmochimica Acta 53, 1583–1595.
Wu, F.Y., Jahn, B.M., Wilde, S.A., Sun, D.Y., 2000. Phanerozoic crustal growth: U–Pb and Sr–Nd isotopic evidence from the granites in northeastern China. Tectonophysics 328, 89–113.
Wu, F.Y., Sun, D.Y., Li, H.M., Jahn, B.M., Wilde, S., 2002. A-type granites in northeastern China: age and geochemical constraints on their petrogenesis. Chemical Geology 187, 143–173.
Wu, F.Y., Jahn, B.M., Wilde, S.A., Lo, C.H., Yui, T.F., Lin, Q., Ge, W.C., Sun, D.Y., 2003a. Highly fractionated I-type granites in NE China (II): isotopic geochemistry and implications for crustal growth in the Phanerozoic. Lithos 67, 191–204.
Wu, F.Y., Walker, R.J., Ren, X.W., Sun, D.Y., Zhou, X.H., 2003b. Osmium isotopic constraints on the age of lithospheric mantle beneath northeastern China. Chemical Geology 196, 107–129.
Wu, F.Y., Walker, R.J., Yang, Y.H., Yuan, H.L., Yang, J.H., 2006. The chemical–temporal evolution of lithospheric mantle underlying the North China Craton. Geochimica et Cosmochimica Acta 70, 5013–5034.
Xu, Y.G., 2001. Thermo-tectonic destruction of the archaean lithospheric keel beneath the sino-korean craton in china: evidence, timing and mechanism. Physics and Chemistry of the Earth, Part A: Solid Earth and Geodesy 26, 747–757.
Xu, Y.G., Menzies, M.A., Thirlwall, M.F., Xie, G.H., 2001. Exotic lithosphere mantle beneath the western Yangtze craton: Petrogenetic links to Tibet using highly magnesian ultrapotassic rocks. Geology 29, 863–866.
Xu, X.S., Griffin, W.L., O'Reilly, S.Y., Pearson, N.J., Geng, H.Y., Zheng, J.P., 2008. Re–Os isotopes of sulfides in mantle xenoliths from eastern China: progressive modification of lithospheric mantle. Lithos 102, 43–64.
Yang, Y.H., Zhang, H.F., Chu, Z.Y., Xie, L.W., Wu, F.Y., 2010. Combined chemical separation of Lu, Hf, Rb, Sr, Sm and Nd from a single rock digest and precise and accurate isotope determinations of Lu–Hf, Rb–Sr and Sm–Nd isotope systems using Multi-Collector ICP-MS and TIMS. International Journal of Mass Spectrometry 290, 120–126.
Yaxley, G.M., Green, D.H., Kamenetsky, V., 1998. Carbonatite Metasomatism in the Southeastern Australian Lithosphere. Journal of Petrology 39, 1917–1930.
Ye, M., Zhang, S.H., Wu, F.Y., 1994. Tectonic units and evolution along the Manzhouli-Suifenhe Geo-profile. Journal of Changchun University of Science and Technology 24, 241–245 (in Chinese).
Zangana, N.A., Downes, H., Thirlwall, M.F., Marriner, G.F., Bea, F., 1999. Geochemical variation in peridotite xenoliths and their constituent clinopyroxenes from Ray Pic (French Massif Central): implications for the composition of the shallow lithospheric mantle. Chemical Geology 153, 11–35.
Zhang, M., Suddaby, P., Thompson, R.N., Thirlwall, M.F., Menzies, M.A., 1995. Potassic rocks in NE China: geochemical constraints on mantle source and magma genesis. Journal of Petrology 36, 1275–1303.
Zhang, M., Zhou, X.H., Zhang, J.B., 1998. Nature of the lithospheric mantle beneath NE China: evidence from potassic volcanic rocks and mantle xenoliths. In: Flower, M.F.J., Chung, S.L., Lo, C.H., Lee, T.Y. (Eds.), Mantle Dynamics and Plate interactions in East Asia, Geodynamics Series: American Geophysical Union, 27, pp. 197–220. Washington D.C.
Zhang, M., Suddaby, P., O'Reilly, S.Y., Norman, M., Qiu, J., 2000. Nature of the lithospheric mantle beneath the eastern part of the Central Asian fold belt: mantle xenolith evidence. Tectonophysics 328, 131–156.
Zhang, J.H., Ge, W.C., Wu, F.Y., Liu, X.M., 2006. Mesozoic bimodal volcanic suite in Zhalantun of the Da Hinggan Range and its geological significance: zircon U–Pb age and Hf isotopic constraints. Acta Geologica Sinica 80, 58–69 (in Chinese with English abstract).
Zhang, L.C., Chen, Z.G., Zhou, X.H., Wang, F., Zhang, Y.T., 2007. Characteristics of deep sources and tectonic–magmatic evolution of the early Cretaceous volcanics in Ganhe area, Da-Hinggan Mountains: constraints of Sr–Nd–Pb–Hf isotopic geochemistries. Acta Petrologica Sinica 23, 2823–2835 (in Chinese with English abstract).
Zhang, Y.L., Ge, W.C., Gao, Y., Chen, J.S., Zhao, L., 2010. Zircon U–Pb ages and Hf isotopes of granites in Longzhen area and their geological implications. Acta Petrologica Sinica 26, 1059–1073 (in Chinese with English abstract).
Zheng, J.P., 1999. Mesozoic–Cenozoic mantle replacement and lithospheric thinning beneath the eastern China. Chinese University of Geosciences Press, Wuhan.
Zhou, Q., Wu, F.Y., Chu, Z.Y., Yang, Y.H., Sun, D.Y., Ge, W.C., 2007. Sr–Nd–Hf–Os isotopic characterizations of the Jiaohe peridotite xenoliths in Jilin province and constraints on the lithospheric mantle age in northeastern China. Acta Petrologica Sinica 23, 1269–1280 (in Chinese with English abstract).
Zhou, Q., Wu, F.Y., Chu, Z.Y., Ge, W.C., 2010. Isotopic compositions of mantle xenoliths and age of the lithspheric mantle in Yitong, Jilin Province. Acta Petrologica Sinica 26, 1241–1264 (in Chinese with English abstract).
Zou, H.B., Zindler, A., Xu, X.S., Qi, X., 2000. Major, trace element, and Nd, Sr and Pb isotope studies of Cenozoic basalts in SE China: mantle sources, regional variations, and tectonic significance. Chemical Geology 171, 33–47.
Zou, H.B., Reid, M.R., Liu, Y.S., Yao, Y.P., Xu, X.S., Fan, Q.C., 2003. Constraints on the origin of historic potassic basalts from northeast China by U–Th disequilibrium data. Chemical Geology 200, 189–201.